MONTAN
UNIVERSITÄT
LEOBEN

Chair of Structural and Functional Ceramics

Master's Thesis

Processing and characterization of alumina – zirconia textured ceramics

Marlies Tabea Wratschko, BSc

September 2021

MONTANUNIVERSITÄT LEOBEN
www.unileoben.ac.at

EIDESSTATTLICHE ERKLÄRUNG

Ich erkläre an Eides statt, dass ich diese Arbeit selbständig verfasst, andere als die angegebenen Quellen und Hilfsmittel nicht benutzt, und mich auch sonst keiner unerlaubten Hilfsmittel bedient habe.

Ich erkläre, dass ich die Richtlinien des Senats der Montanuniversität Leoben zu "Gute wissenschaftliche Praxis" gelesen, verstanden und befolgt habe.

Weiters erkläre ich, dass die elektronische und gedruckte Version der eingereichten wissenschaftlichen Abschlussarbeit formal und inhaltlich identisch sind.

Datum 20.09.2021

Unterschrift Verfasser/in
Marlies Tabea Wratschko

erc

European Research Council

Established by the European Commission

Funding for this research was provided by the European Research Council (ERC) excellent science grant “CERATEXT” through the Horizon 2020 program under contract 817615.

Acknowledgements

An erster Stelle möchte ich mich bei meinem Betreuer und Vorstand des Instituts für Struktur – und Funktionskeramik Univ. – Prof. Dr. Raul Bermejo für die Ermöglichung dieser Arbeit inmitten der Pandemie, sowie für die hervorragende Betreuung bedanken. Seine stets offenen Türen um nach fachlichen Rat zu fragen und speziell das Begutachten Teile meiner Arbeit auch in seiner Freizeit, möchte ich ihm besonders hoch anrechnen.

Ein ganz besonderer Dank geht an meine zweite Betreuerin Dipl. – Ing. Anna – Katharina Hofer für ihre bedingungslose Unterstützung, die perfekte Organisation und für das mir entgegengebrachte Vertrauen. Ich fühlte mich zu keiner Zeit alleine gelassen und hätte mir keine bessere Betreuung wünschen können.

Ein herzliches Dankeschön möchte ich auch an Dipl. – Ing. Josef Schlacher und Dipl. – Ing. Irina Kraleva richten, die stets als Ansprechpartner bei experimentellen Arbeiten fungierten und sofort zur Hilfe eilten, wenn diese benötig wurde. Weiters möchte ich mich bei Ing. Ronald Binder bedanken, der meine Proben immer schnellstens möglich mechanisch bearbeitet hatte und sich dadurch nie lange Leerlaufphasen ergaben. Ein genereller Dank ist dem gesamten Mitarbeiterteam des Instituts für Struktur – und Funktionskeramik ausgesprochen für das überaus angenehme Umfeld und die allgemeine Hilfsbereitschaft.

Mein größter Dank gilt meinen Eltern, Silvia und Andreas, die mir überhaupt mein Studium ermöglicht haben, mich finanziell, aber noch viel wichtiger, auch mental jederzeit unterstützt haben. Sie haben mir die nötige Liebe und Geborgenheit geschenkten und mich immer wieder im Glauben an mich selbst bestärkt. Ein großes Dankeschön ist an meinen Bruder Markus gerichtet, der sich im Laufe meines Studiums stets meinen ID – technischen Problemen angenommen hat.

Abschließend möchte ich meinem Freund Gerald einen besonderen Dank aussprechen, für seine beruhigende Art, seinen immerzu guten Rat und dass er mir allezeit den nötigen Rückhalt geboten hat. Auch meinen Freunden möchte ich danken, dass sie mir immer ein Lächeln ins Gesicht gezaubert haben, mir Momente der Auszeit des Alltags schenkten und immer für jede Prüfungsphase vollstes Verständnis zeigten.

Abstract

The bio – inspired “brick and mortar” concept has proven to be an effective way to enhance damage tolerance in ceramic – based materials. Based on the phenomenon of crack shielding, bifurcation and deflection, caused by the preferred orientation of the microstructure, energy is dissipated during crack propagation. This results in an improved fracture behavior.

This thesis focusses on the fabrication and characterization of textured alumina (TA) composites, aiming to understand how a second phase influences the development of texture as well as the physical and mechanical properties of the composite material.

Monolithic textured alumina with SiO_2 + CaO as sintering additives, was fabricated utilizing the tape casting process for grain alignment, followed by templated grain growth (TGG) during sintering. In addition, a variety of compositions of textured alumina containing 0.5 vol% – 20 vol% of monoclinic zirconia (m-ZrO_2) were prepared. Both the reference and composite materials were characterized according to their microstructure, physical and mechanical properties. The degree of texture was determined using microstructural and XRD analysis. The hardness was measured after Vickers and the fracture toughness by using the Single Edge V – Notched Beam method (SEVNB).

In order to better understand the effects of texture on their damage tolerance behavior in ceramic materials, monolithic textured alumina samples were tested perpendicular as well as parallel to the basal surface of the oriented direction grain basal surface. Anisotropic fracture behavior was observed with slightly higher toughness for the testing orientation perpendicular to the basal planes. The composite materials were only tested perpendicular to the grain orientation. Whereas for pure TA and TA with small contents (0.5 vol%) of second phase, intergranular fracture was observed, increasing zirconia content (beyond 1 vol%) led to transgranular fracture. It was found that with increasing volume fraction of the second phase, the templates are hindered from growing, resulting in the loss of texture. High quality of preferred grain orientation was only achieved for compositions containing up to ≈ 2 vol% m-ZrO_2. Furthermore, higher relative density was obtained with increasing second phase, however with a detrimental effect on fracture resistance and a change in Vickers hardness. The finding of this thesis opens the possibility of fabricating textured alumina with incorporation of a second phase, aiming to tailor density, hardness and fracture resistance, based on the final application pursued.

Keywords: textured alumina / second phase reinforcement / templated grain growth (TGG) / tape – casting / damage tolerance

Kurzfassung

Das bioinspirierte „Brick and Mortar“ – Konzept hat sich als eine effektive Strategie bewährt, die Schadenstoleranz von keramischen Werkstoffen zu verbessern. Die Theorie basiert auf Energie – Dissipation, gewährleistet durch Rissablenkungen, Verzweigungen oder Rissstopp während des Risswachstums in einem Gefüge mit bevorzugter Kornorientierung. Dies führt zu einem verbesserten Bruchverhalten und einem Anstieg der Bruchzähigkeit in Keramiken.

Diese Arbeit konzentriert sich auf die Herstellung und Charakterisierung von (i) monolithischem texturierten Aluminiumoxid (TA) und (ii) Verbundwerkstoffen, mit dem Ziel; den Einfluss einer zweiten Phase auf texturiertes Gefüge hinsichtlich Texturentwicklung, sowie die daraus resultierenden physikalischen und mechanischen Eigenschaften, zu untersuchen.

Für die Herstellung von monolithischem texturierten Aluminiumoxid mit SiO_2 + CaO als Flüssigphasenzusatz, wurde das „Tape Casting“ Verfahren verwendet. Das endgültige Gefüge wurde mittels der Methode des „Templated Grain Growth“ (TGG) während des Sintervorgangs realisiert. Zusätzlich wurden Verbundwerkstoffe mit Aluminiumoxid und unterschiedlichen Zusammensetzungen von 0,5 Vol.% – 20 Vol.% monoklinem Zirkonoxid (m-ZrO_2) hergestellt. Sowohl das monolithische Material als auch die Verbundwerkstoffe wurden auf das Gefüge, deren physikalischen und mechanischen Eigenschaften charakterisiert. Die Qualität der Textur wurde mittels XRD Messungen bestimmt. Die Härte wurde mit dem Härteprüfverfahren nach Vickers und die Bruchzähigkeit mit der Single Edge V – Notched Beam Methode (SEVNB) gemessen.

Um zu verstehen, wie sich eine Textur in einem keramischen Werkstoff auf z.B die Schadenstoleranz auswirkt, wurden die monolithischen Proben sowohl senkrecht als auch parallel zur Grundfläche der bevorzugten Kornorientierung auf ihre Bruchzähigkeit geprüft. Dabei wurde anisotropes Bruchverhalten beobachtet. Die senkrecht orientierten Proben wiesen jeweils höhere Bruchzähigkeitswerte auf. Die Verbundwerkstoffe wurden ausschließlich senkrecht zur Kornorientierung getestet. Interkristallines Bruchverhalten konnte für reines TA und TA mit geringem Zirkonoxid – Gehalt (0,5 Vol.%) beobachtet werden. Mit höherem Volumsanteil an zweiter Phase (ab 1 Vol.%), wurde transgranulare Rissausbreitung festgestellte. Weiters konnte beobachtet werden, dass mit zunehmendem Anteil an zweiter Phase die Textur in den Verbundwerkstoffen abnimmt. Dies ist auf die Behinderung des Kornwachstums während der Gefügeausbildung zurückzuführen. Ein hoher Orientierungsgrad wurde bis ≈ 2 Vol% m-ZrO_2 erreicht. Darüber hinaus wurde mit zunehmender zweiter Phase eine höhere relative Dichte und eine Verbesserung der

Vickers – Härte erzielt, jedoch auch eine nachteilige Wirkung auf die Bruchfestigkeit. Die Ergebnisse dieser Arbeit bieten die Möglichkeit, durch den Einbau einer zweiten Phase in texturiertes Aluminiumoxid, maßgeschneiderte Dichte, Härte als auch Zähigkeitseigenschaften herzustellen.

Schlagwörter: texturiertes Aluminiumoxid / Phasenverstärkung / Templated Grain Growth (TGG) / “Tape Casting” Prozess / Schadenstoleranz

Table of Contents

List of Abbreviations

Abbreviation	**Description**	**Unit**
TA	Textured alumina	
EA	Equiaxed alumina	
ZTA	Zirconia – toughened Alumina	
m-ZrO_2	Monoclinic zirconia	
TGG	Templated grain growth	
LPS	Liquid Phase Sintering	
LF	Lotgering Factor	-
f	Textured volume fraction	-
r	Orientation parameter	-
FWHM	The Full Width at Half Maximum	°
XRD	X-ray diffraction	
SEVNB	Single Edge V – Notched Beam	
SEPB	Single Edge Precracked Beam	
K_{IC}	Fracture toughness	$\mathrm{MPa\ m^{1/2}}$
Y^*	Non – dimensional geometrical factor	
HV	Vickers hardness	
CTE	Coefficient of thermal expansion	$\mathrm{K^{-1}}$
E	Young’s modulus	GPa
SEM	Scanning electron microscope	
LIMI	Optical Light Microscope	
m	Weibull modulus	-

1. Introduction

1.1. Background

The continuous progress in advanced technologies is followed by the need to constantly develop high performance materials. According to engineering applications, ceramics are of high interest due to their outstanding structural as well as functional properties. Regarding structural properties, ceramic materials exhibit low specific density, high wear resistance as well as chemical and thermal stability. Structural ceramics typically show high hardness as well as stiffness. Under compression they can withstand high loads. Regarding their functional properties, ceramics are often selected as optimal material, due to their electrical conductivity/resistance, piezo – electricity, optical characteristics and thermal conductivity/resistance. [1,2]

Despite their outstanding properties, the use of ceramics is still restricted for numerous applications because of their brittle character. The catastrophic fracture behavior results from the strong directional bonding between the atoms in the material, which can be ionic, covalent or a combination of both. In contrast to metals, which are able to reduce local stress peaks through plastic deformation, ceramics are able to dissipate only small amount of energy in plastic flow, because of their high yield strength. [2]

Furthermore, ceramics are limited in use because their mechanical strength is strongly determined by size, orientation and distribution of defects in the material. Manufacturing ceramics without defects is very challenging, because they are intrinsic to processing, or are easily introduced at handling and post machining as well as in service. Each flaw is a potential source for crack initiation and the size and location of the critical defect can be different within every sample. As a consequence, mechanical strength in ceramics is usually described by a distribution function evaluated using Weibull statistics. [3]

Additionally to the scatter in strength, ceramics may suffer from sub – critical crack growth (SCCG) of initial defects which results in delayed failure. Caused by constant applied loads, even lower than predicted by Weibull theory, sudden crack propagation can occur without warning, far after the first application of load. This process is also called “stress corrosion” and is influenced by humidity and temperature. [4] Furthermore, ceramics are also very sensitive to rapid changes in temperature, especially rapid cooling, leading to thermal shock cracks, especially at the surfaces. [2]

The current challenge is to make ceramics more reliable, achieved by fulfilling the requirements on high strength and toughness to ensure a certain “damage – tolerance”. Unfortunately, these mechanical characteristics are usually mutually exclusive in many materials. That is the reason why traditionally the development of strong and simultaneous tough materials for specific engineering applications is always a compromise between hardness versus ductility. Therefore, for safety, critical applications where catastrophic failure is unacceptable, in most cases a lower strength material is employed, and hence higher toughness. Softer materials can deform more readily and are able to undergo a limited deformation. This enables a local dissipation of high stresses. Hard materials show a rather brittle character, attributed to a higher yield stress compared to fracture stress, which as a result leads to failure before yielding. [5]

In exchange, several strategies have been adopted to improve strength and toughness. Applied strengthening mechanisms are based on the one hand on reducing or even eliminating intrinsic defects from processing, by utilizing colloidal processing routes. Thus, leading to a reduction of the scattering in strength, allowing the fabrication of advanced ceramics. [6] On the other hand, the strengthening route can be based on preventing the material from defects introduced at handling, by generating compressive residual stresses at the surface. This can be performed by using an ion exchange process [7], like it is well known from the popular Gorilla® glass [8].

Strengthening approaches are rather based on inhibiting crack initiation. Since flaws on the surface are difficult to be avoided in service, a better strategy is to enhance toughness in order to improve “flaw tolerance”. Some concepts have been investigated using energy – dissipation to impede crack propagation. For instance, the addition of ceramic fibers, whiskers or platelets into a ceramic microstructure may cause toughening mechanisms as crack bridging and frictional pull – outs. Further, the manipulation on macroscopic scale by creating layers with different properties to reach high strength or stiffness; or to fabricate hybrid layers with different materials; as well as self – reinforcement by forming a texture, are popular tools to enhance toughness. [9] Materials with such toughening mechanisms can exhibit an R – curve behavior, where the resistance against crack propagation increases with crack extension. [10]

Materials with a pronounced R – curve behavior can be found in nature, as bones, dentin or nacre. Highly sophisticated and complex hierarchical structures over many dimensions are reported to be responsible for an outstanding fracture behavior. [11] Considering nacre from the mollusc shell, it can exhibit unique characteristics of high toughness and strength, although it is a rather brittle inorganic material. Their extraordinary properties can be related to extrinsic as well as intrinsic toughening mechanisms, acting at different length scales. [12] The structure of nacre is described as “brick and mortar” structure, which consists of more than 95 % vol. of calcium carbonate platelets working as “bricks” with small amounts of soft organic phase (0.01 % – 5 wt.% by mass) as “mortar” in between. [13] That small percentage of biopolymers can lead to a significant enhancement in mechanical properties. Because of the large difference in stiffness, the crack is prone to propagate in the organic phase. This so – called “shear lag model” results in a higher toughness and strength of the structure, in comparison to the individual components. [14]

The knowledge that a hierarchical textured microstructure can significantly influence the mechanical behavior, has led to numerous studies on finding methods with the opportunity of replicating such complex designs in a synthetic way. The objective is to build a texture, e.g. a nonrandom grain alignment, to achieve properties only known from single crystals, while also possessing the mechanical robustness of a bulk material.

In this relation, it has to be noted that texture may not only improve structural properties as a better damage – tolerance, it may also be an important tool for the enhancement of magnetic, ferroelectric, thermoelectric and superconducting properties. [15] However, this is beyond the scope of this thesis, which will rather focus on structural reinforcement.

1.2. Aims and objectives

The aim of this thesis is the processing and characterization of (i) monolithic textured alumina and (ii) textured alumina reinforced with a second phase. Regarding (i), monolithic textured alumina (TA) will be fabricated using the tape casting process. For the understanding of the effect of toughening mechanisms on the fracture behavior due to aligned grains, TA will be characterized according to its microstructure, its physical and mechanical properties.

The question to be answered is how a second phase will influence the textured material. According to (ii) monoclinic zirconia (m-ZrO_2) will be added in various contents to TA. One hypothesis is that due to mismatching coefficients of thermal expansion of TA and m-ZrO_2, intrinsic residual compressive stresses are induced. This may lead to an improvement of the resistance against crack propagation. Additionally, it is hypothesized that due to volume increase of zirconia occurring due to the phase transformation from tetragonal to monoclinic, additional intrinsic residual compressive stresses may enhance the fracture behavior as compared to the bulk TA material.

Furthermore, a second phase in textured alumina may affect the development of texture during sintering and as a consequence its physical and mechanical properties. In this regard, a variety of contents (0.5 vol% - 20 vol%) of m-ZrO_2 will be added to TA to tailor its hardness and fracture toughness. The degree of texture will be determined using microstructural and XRD analysis. The hardness will be measured after Vickers and the fracture toughness using the Single Edge V – Notched Beam method (SEVNB).

This thesis is structured as followed: Chapter 2 is dedicated to the literature research, where the concept as well as the processing strategy of textured engineering ceramics is reviewed. In chapter 3, the experimental procedure is described, detailing the materials of study, a processing part and a microstructural and mechanical characterization part. Results and discussion are given in chapter 4, followed by the conclusion and outlook on further research based on the experimental findings.

2. State of the Art

2.1. Textured engineering ceramics

For most structural applications, a specific strength and toughness are essential. While properties of the ceramic materials are mainly determined by their microstructure, novel researches concentrate on the design of textured microstructures, using bioinspired concepts. An object of interest is nacre from the mollusc shell, because of its specific hierarchical layered structure (see Fig. 1). The material exhibits outstanding fracture resistance based on the combination of “intrinsic” and “extrinsic” toughening mechanisms acting at different length scales. [16] Recently, the mission of scientists has been devoted to mimic these “brick and mortar” architectures.

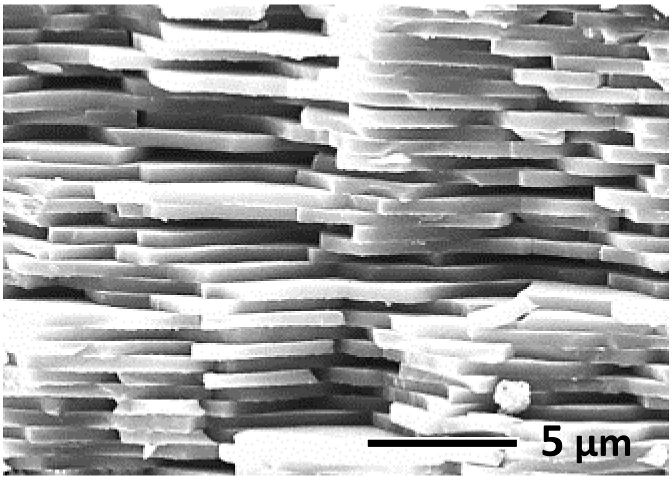

Fig. 1: *SEM micrographs of nacre (cross – section) [17]*

Over the years, researchers have investigated several “brick and mortar” combinations to achieve enhanced structural properties. For example, F. Bouville et al. used 2 vol% Al_2O_3 bridges and $9Al_2O_3 \cdot 2B_2O_3$ acting as the ”mortar” material [12], where they achieved a fracture toughness of $K_{IC} = 7.4 \pm 1.5$ MPa $m^{1/2}$; almost two times higher than evaluated for equiaxed monolithic alumina. By utilizing 2 vol% dopants of Al_2O_3 bridges and $SiO_2 + CaO$ glass, K_{IC} values as high as 5.9 ± 0.6 MPa $m^{1/2}$ have been measured [12]. However, it has to be mentioned that the performance of a material dependents on its fabrication process.

Five general main techniques that have been exploited in the last few years for manufacturing textured microstructures are (i) the Rolling Assisted Biaxially Textured Substrates process (RABiTS) [18], (ii) powder – in – tube (PIT) [19], (iii) strong (7–14 T) magnetic field alignment

(MA) of particles [20], (iv) reaction templated grain growth (RTGG) and (v) templated grain growth (TGG) [21,22]. Applying these techniques enables to fabricate samples with a textured volume fraction of up to 90%. [15]

2.1.1. Methods of grain alignment

One of the first techniques which was established to induce a preferred grain orientation in a ceramic microstructure was the magnetic alignment (MA), developed in the 1950s. Rathenau et al. [23] fabricated textured $BaFe_{12}O_{19}$ by applying a magnetic field during the powder compaction process for aligning the plate – like $BaFe_{12}O_{19}$ particles. A strong [001] orientation parallel to the direction of the magnetic field has been reported. In the course of time a large number of powder or sol – gel processes have been evolved, categorized by mechanical, electromagnetic, or thermal driving forces. [15]

S. Deville et al. [24] researched on preferred platelets orientation in materials caused by thermal driving forces utilizing ice – templating. In this method high aspect ratio ceramic platelets are dispersed in a solvent, usually water. While decreasing the temperature, water crystals nucleate and grow along the temperature – gradient. Through the crystallizing of water in a tailored direction, also the ceramic particles are oriented. The ice – crystals are than removed by sublimation. The results are mainly macroporous and cellular structures, as well as bulk material with a high relative density. In addition, the morphology of the crystals can be influenced by applying electric field during crystallization improving the grain alignment.

F. Bouville et al. [12] investigated the fabrication of nacre – like aluminas (NLAs) by utilizing different processing techniques, as (i) ice – templating, (ii) magnetically assisted slip casting (MASC) [25] and (iii) hot pressing [26]. The fabricated green bodies were sintered using the field assisted sintering technique (FAST). It was shown that each process influences the microstructure regarding platelet alignment as well as the composition of the interfaces according to the “brick and mortar” structure. In any call a delayed crack propagation resistance has been reported for each material and process of study, leading to a higher fracture toughness in comparison to monolithic equiaxed alumina, as already mentioned above.

2.1.2. Processing textured microstructure using tape casting process

Mechanical preferred orientation of templates can be achieved via the tape casting process. A previous work by R.J. Pavlacka et al. [27] and A. – K. Hofer et al. [28] showed that textured monolithic alumina exhibits a higher damage tolerance (K_{IC} (TA) = 4.6 MPa $m^{1/2}$) in comparison to equiaxed alumina (K_{IC} (EA) = 3.3 MPa $m^{1/2}$ [29]). This may be attributed to occurring crack deflection mechanisms caused by the preferred oriented microstructure; thus leading to an increase in fracture toughness due to energy dissipation during crack propagation.

Via the tape casting process also called “fluid forming process”, ceramic tapes of thicknesses ranging from 1 µm to 3 mm can be produced. During slurry preparation the ceramic powder and the polymer binder are homogenized in a solvent system. The system can either be based on aqueous or non – aqueous solvents. [30]

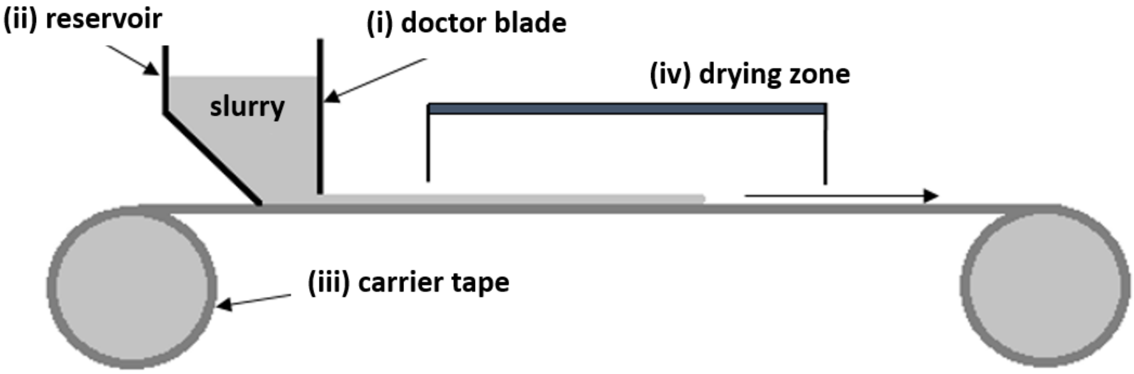

Fig. 2: *Schematic of the tape casting process*

The main components of a tape caster are the (i) stationary doctor blade, (ii) the reservoir, (iii) a moving carrier tape (mylar©) and (iv) a drying zone (see Fig. 2). With the height of the doctor blade, the thickness of the tape can be adjusted. Through the movement of the carrier tape, the slurry from the reservoir is applied. Along the heated drying zone, the solvent evaporate, resulting in a dried flexible tape consisting of ceramic powder embedded in a polymer binder matrix. Regarding the textured microstructures, templates are aligned through occurring shear stresses due to the resistance of motion of the slurry passing the doctor blade. The gradient of this shear stress leads to a torque causing the orientation of platelets get orientated parallel to the movement. [31] The magnitude of the occurring shear forces are influenced by different parameters, such as the slurry viscosity, the velocity of casting as well as the gap height between the doctor blade and the moving carrier tape. [32]

2.1.2.1 Templated Grain Growth (TGG)

Templated grain growth (TGG) is a method applied to generate texture in ceramic microstructures due to *Ostwald ripening.* Whereas high aspect ratio templates are used to serve as epitaxial nuclei of similarly oriented grains (see Fig. 3), the submicron – sized powder matrix is the source for the process of dissolution and precipitation. The driving force in this process is the minimization of surface energy. [33] Here, the energy is lowered through the reduction of interfacial area between the precipitates and the medium. Since the surface tension of smaller particles is comparably higher than that of bigger particles, they “dissolve” and “precipitate” onto large templates, minimizing the energy. As a result anisotropic growth of the templates occurs, leading to a structure of elongated grains, which in the case of α-alumina, corresponds to an orientation of the basal plane (0001) parallel to the sample surface [15,34].

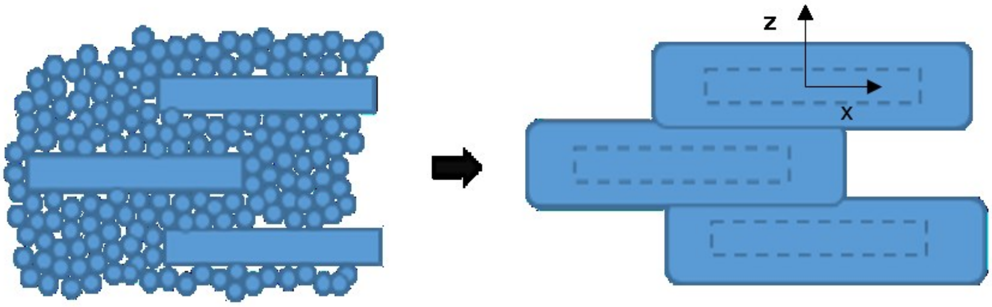

Fig. 3: *Schematic of Templated Grain Growth [15]*

2.1.2.1.1 Sintering of textured ceramics: Liquid Phase Sintering (LPS)

Liquid phase Sintering (LPS) is typically used for materials with a high degree of covalent bondings, as found in hard materials with a high melting point. In comparison, solid – state sintering (SSS) of such materials, would lead to rather porous structures, due to weak densification. In addition, due to the high melting points, very high temperatures would be needed for SSS, relating to high costs. Using LPS diffusion mechanisms can be activated already at lower temperatures, making it possible to fully densify hard materials at a lower expense. However, the enhancement of diffusivity might also lead to abnormal grain growth. In the case of TGG and the development of large elongated grains, abnormal grain growth and *Oswald ripening* is desired. Therefore, the method of Liquid Phase Sintering (LPS) is utilized for the fabrication of textured microstructures.

For LPS, sintering additives are mixed with the ceramic powder during processing, which form a liquid phase during sintering. Through the liquid phase, the dissolution and precipitation of small particles is reinforced, provoking an enhanced growth of particles.

In general, liquid phase sintering can be categorized in three stages:

Stage 1:
At the beginning of sintering, the sintering additives are still solid. With increasing temperature, they start to liquefy and wet the particles. A good wettability of the liquid phase onto the ceramic particles is a fundamental requirement (see Ref. [35] for more detail) for successful LPS. Through the distribution of the liquid phase within the particles, capillary forces occurr, causing the rearrangement of the particulate solids. The capillary pressure *p* can be evaluated for an idealized system using equation (1):

$$p = \gamma_{lv}\left(\frac{1}{R} - \frac{1}{r}\right) \tag{1}$$

where γ_{lv} is the surface tension, *R* and *r* are the principal radii of curvature of the meniscus formed by the liquid.

Stage 2:
In this stage the dissolution and precipitation of matter occurs, which is controlled by the diffusivity in the liquid phase. It can be said that the diffusion rate in liquid state is generally higher than in solid state. Ceramic powder particles with a higher chemical potential start to dissolve at the solid – liquid interfaces. The dissolved matter migrates to a closer particle and precipitates on its surface with lower chemical potential; densification and grain growth takes place. For systems with a distribution of particle sizes, the matter is typically transported from smaller to a larger particles resulting in *Ostwald ripening*. Due to the mentioned capillary forces, particles are pulled together, enhancing dissolution, resulting in a modification of particle shape; they become flat.

Stage 3:
During the final stage, sintering is controlled by the densification of the solid particulate skeleton network and dominated by *Ostwald ripening*. In this stage, pores are aimed to be closed due to particle growth, offering the possibility to fabricate a fully dense material. [35,36]

3. Experimental Work

3.1. Materials of Study

In this work, (i) monolithic textured alumina (TA) as well as (ii) TA with different contents of monoclinic zirconia (m-ZrO_2) was fabricated using the tape casting process. First monolithic TA was processed and characterized according to its microstructure, physical and mechanical properties. Further, TA with selected volume fractions of m-ZrO_2 as a second phase 0.5 vol%, 1.0 vol%, 2.0 vol%, 5.0 vol%, 10.0 vol% and 20.0 vol%, were fabricated, the microstructure analyzed and the hardness as well as the fracture toughness determined. Alumina has been used for numerous investigations on texturing ceramic microstructures. Considering the introduction of zirconia as second phase in alumina, typically tetragonal zirconia is used due to its property of transformation toughening, as e.g. Zirconia – toughened Alumina (ZTA) [37]. However, in this thesis monoclinic zirconia will be added to textured alumina, aiming to control hardness, fracture toughness and the degree of texture.

3.1.1. Aluminium oxide (= alumina, Al_2O_3)

Alumina, extracted from Bauxite via the Bayer – Process, is one of the most important structural ceramics. It exhibits high – temperature stability and the retention of strength at high temperatures [38]. Alumina can occur in different allotropic forms whereas the α-phase, also called corundum, is the most common and widely used for industrial applications. Fig. 4 shows the crystal structure of α-Al_2O_3, consisting of large oxgen ions (O^{-2} anions) in an hexagonal close packed arrangement with small aluminum ions (Al^{+3} cations) occupying two – thirds of the octahedral interstices. The α-Al_2O_3 has a relative high hardness with HV10 ≈ 19 GPa, but a relatively low fracture toughness (K_{IC} = 3-4 $MPm^{1/2}$). Considering an α-alumina single crystal, the properties are anisotropic, e.g. the (0001) plane (basal plane) of the hexagonal lattice exhibits a higher hardness in comparison to the prismatic planes. Its coefficient of thermal expansion (CTE) measured normal to [0001] direction (CTE) is $\alpha = 8.3 * 10^{-6}$ 1/K and parallel to the a-axis as high as $9.0 * 10^{-6}$ 1/K. [39,40]

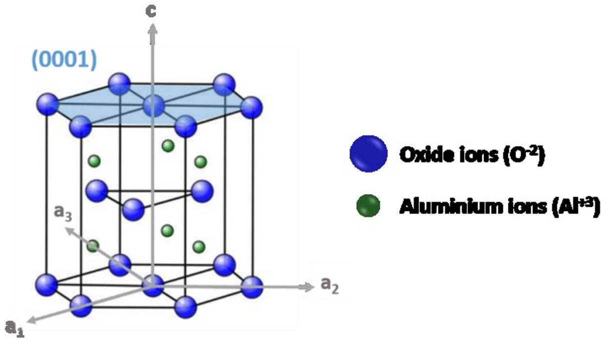

Fig. 4: Hexagonal crystal structure of α-alumina

3.1.2. Zirconium dioxide (= zirconia, ZrO_2)

Besides alumina, zirconia is commonly used for technical as well as in medical applications. Zirconia develops three different crystal structures throughout different temperature ranges as displayed in Fig. 5. Monoclinic zirconia (m), stable at room temperature, is rarely used as bulk material because of its brittle character; it is rather used as thin film coatings or as an alloy. At a temperature > 1170 °C zirconia transforms without diffusion (martensitic transformation) into the tetragonal phase (t), which is accompanied with a volume decrease of 5-8 %.

Fig. 5: *Schematic phase transformation of zirconia*

Due to the phase transformation toughening mechanism from tetragonal to monoclinic zirconia, it is desired to stabilize zirconia in its tetragonal phase. Therefore, dopants as Yttriumoxide (Y_2O_3) are used, to occupy positions of Zr^{+4} ions with Yttrium ions (Y^{+3}) and inducing oxygen – vacancies, prohibiting the t → m transformation during cooling and stabilizing the tetragonal phase. The mechanical characteristics vary for the different crystal structures. Whereas a single crystal of monoclinic zirconia reaches a hardness of 6.6 GPa [41], for polycrystalline tetragonal zirconia the hardness has been reported to be ≈ 12 GPa [29]. According to the fracture toughness of polycrystalline zirconia, monoclinic zirconia exhibits a fracture toughness of ≈ 2 $\text{MPa}\,\text{m}^{1/2}$ [41], in comparison to tetragonal zirconia with K_{IC} ≈ 5-10 $\text{MPam}^{1/2}$ [29]. The CTE of the monoclinic structure was found to be $\alpha = 6.8\text{-}8.4 * 10^{-6}$ 1/K, tested parallel to the a-axis, whereas for the tetragonal phase it is in the range of 8-10 * 10^{-6} 1/K [1].

3.2. Processing of textured alumina – zirconia composites

3.2.1. Slurry preparation and formulation

Table 1 shows the formulations for all fabricated samples with different volume fractions of added monoclinic zirconia (m-ZrO_2). Following Table 1, first the alumina powder (α-Al_2O_3 99.99% ultrafine, TM-DAR, Taimei Chemicals Co., Ltd., Nagano, Japan) and the monoclinic zirconia contents (0-20 vol%) (m-ZrO_2, TZ-0Y, Tosoh, Tokyo, Japan), were weighted into a ball – mill bottle (PE – bottle) together with 80 % of the solvents Ethanol 99% (Sigma – Aldrich, Darmstadt, Germany) and Xylene (Avantor Performance Materials Poland S.A., Gliwice, Poland), the LP – sintering additives CaO (in form of $Ca(NO_3)2\text{-}4H_2O$, ThermoFisher GmbH, Kandel, Germany) and SiO_2 (in form of $C_8H_{20}O_4Si$, ThermoFisher GmbH, Kandel, Germany), as well as the dispersant (Menhaden fish oil, Sigma – Aldrich Handels GmbH, Vienna, Austria). The characteristics and the quality of the ceramic powder are fundamental for generating highest possible green density and correspondingly sintered bulk density. Considering the solvents, they are responsible for the dissolution of the organic components as well as the uniform distribution of powder particles and other additives. Here, a system of non – aqueous solvents is utilized, which was selected because of a rather rapid evaporation during the tape casting process. The LP sinter dopants, forming the liquid phase during sintering, are added to enhance *Ostwald ripening* during TGG. The applied Menhaden fish oil acts as a Surfactant ("SURFace ACTive AgeNT"), dispersing and separating the particles due to steric hindrance in the viscous slurry.[30] For ball – milling, the PE – bottle was additionally filled to a 1/3 with alumina beads (5 mm in diameter). The suspension was mixed for 24 h on the ball – mill with a rotation speed of 30 min^{-1}. After 24 h the binder (Polyvinylbutyral, Sigma – Aldrich Chemie GmbH, Steinheim, Germany) and the plasticizers (Butylbenzyl Phthalate, Sigma – Aldrich Chemie GmbH, Steinheim, Germany and Dibutyl sebacate, Sigma-Aldrich Chemie GmbH, Steinheim, Germany) were added and ball – milled for another 24 h. The binder provides the network, holding the powder particles together in the dried tape. In addition to the binders, plasticizers are used to modify the glass – transition temperature and the chain length of the binder to guarantee a certain flexibility, plasticity and workability of the green tape at room temperature. [30]

Before sieving the slurry out of the ball – mill bottle, first α-alumina templates have to be added and mixed with the prepared slurry. Here, the α-Al_2O_3 templates (Rona Flair® White Sapphire, EMD Performance Materials Corp., Darmstadt, Deutschland) with a thickness of ≈ 0.10 µm and a diameter of ≈ 5-16 µm, were dispersed with 0.2 g of dispersant in the remaining 20 % of solvents (Ethanol 99% and Xylene) followed by ultra – sonication. Following, they were added to the ceramic slurry and ball – milled for 30 min.

The slurry was then sieved into a beaker and 3 drops of cyclohexanone (ThermoFisher GmbH, Kandel, Germany) were added. Cyclohexanone is acting as a homogenizer; it keeps the tape surface liquid, and thus avoiding skin formation during drying. Thereby it facilitates the diffusion of other solvents through the tape enhancing a homogeneous evaporation [30]. The beaker was covered with a parafilm© and the slurry stirred on a magnetic stirrer for 24 h for the removal of trapped air.

Table 1: *Slurry formulations for all samples with different volume fractions of monoclinic zirconia*

vol% m-ZrO_2		**0.0** [vol%]	**0.5** [vol%]	**1.0** [vol%]	**2.0** [vol%]	**5.0** [vol%]	**10.0** [vol%]	**20.0** [vol%]
Solids	Al_2O_3 (Taimei)	18.102	17.933	17.810	17.564	16.839	15.665	13.439
	m-ZrO_2	0.000	0.095	0.189	0.377	0.933	1.832	3.537
	Al_2O_3 (templates)	0.905	0.944	0.937	0.924	0.886	0.824	0.707
LP-Sintering	$Ca(NO_3)_2\text{-}4H_2O$	0.081	0.081	0.081	0.081	0.082	0.082	0.083
	$C_8H_{20}O_4Si$	0.145	0.145	0.146	0.146	0.146	0.147	0.148
Solvents/ Dispersant	Fish oil*	2.608	2.609	2.610	2.612	2.619	2.630	2.650
	Xylenes	33.151	33.165	33.180	33.209	33.294	33.432	33.693
	Ethyl Alcohol	36.071	36.087	36.103	36.134	36.227	36.377	36.661
Binder/ Plasticizer	Polyvinyl Butryal	5.058	5.060	5.062	5.066	5.079	5.100	5.140
	Butylbenzyl Phthalate	2.258	2.259	2.260	2.262	2.268	2.277	2.295
	Dibutyl sebacate	1.621	1.622	1.622	1.624	1.628	1.635	1.648
	3 drops cyclohexanone							
	0.2 g Fish oil* (platelets)							

3.2.2. Viscosity measurement

Before the tape casting process, the viscosity (η) of the slurry was determined with a viscometer, type: ViscoQC 300 (Anton Paar, Graz, Österreich) using the L3 – tool. A constant rotation speed of 250 rpm for 1 min was used to evaluate η. The viscosity should be in the range of 250 and 350 mPas for a well alignment of the templates during the tape casting process.

3.2.3. Tape Casting process

The tape casting process was performed with the Tape Caster CAM-L (Keko Equipment Ltd., Žužemberk, Slowenien) (see chapter 2.1.2 Processing textured microstructure using tape casting process). The thickness of the tape was determined by the gap height between the doctor blade and the moving carrier tape (mylar©). The gap height was set to 250 µm. The slurry was filled into the reservoir and applied on the mylar© by moving with a constant speed of 0.35 m/min. In the heating chamber the solvents were evaporated through a three zone temperature profile (1st zone: 30 °C, 2nd zone: 45 °C, 3rd zone: 35 °C).

3.2.4. Cutting and Lamination

For the fabrication of samples, the tapes, with a dry thickness of ≈ 50 µm, were cut into squares with the dimensions of 55 x 55 mm (see Fig. 6 a)). The separate layers were stacked to a total thickness of 4 mm (Fig. 6 b) and c)).

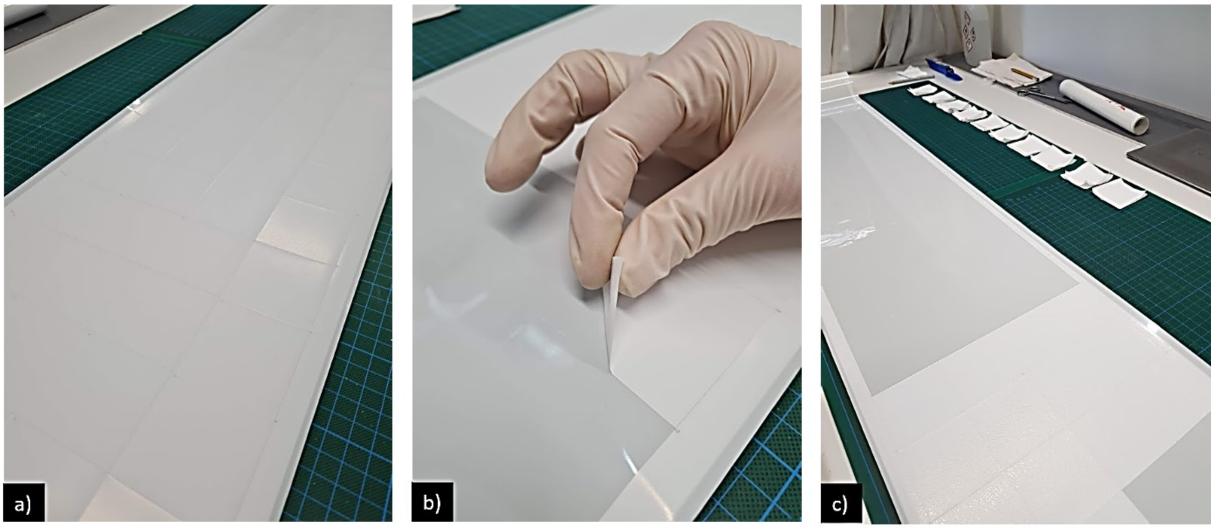

Fig. 6: *Cutting and lamination steps of the sample manufacturing: a) cutting squares, b) pull – off from carrier tape, c) stacking*

3.2.4.1 Uniaxial pressing

For lamination, the stacked layers were first warm uniaxial pressed by using a universal testing machine (MIDI 10-5/6x11, Messphysik Materials Testing GmbH, Fürstenfeld, Österreich) with a two – zone controller (Controller EDC 580, DOLI Elektronik GmbH, Münsingen, Deutschland). The uniaxial pressing was performed at a temperature of 75 °C with a constant load of 19.3 kN for 15 minutes.

3.2.4.2 Isostatic pressing

After uniaxial pressing, the samples were vacuum – sealed and isostatically pressed (ILS-46, Keko Equipment Ltd., Žužemberk, Slowenien) at a temperature of 75 °C and a pressure of 20 MPa for 30 minutes.

3.2.5. Binder – burn – out

The binder system was removed in a convection furnace (Thermconcept GmbH, Bremen, Deutschland) with (a) a heating rate of 0.3 °C/min to 600 °C, (b) a dwell time of 2 hours, (c) a first cooling rate of 0.8 °C/min to 400 °C and (d) a second cooling rate of 3 °C/min to room temperature (see Fig. 7).

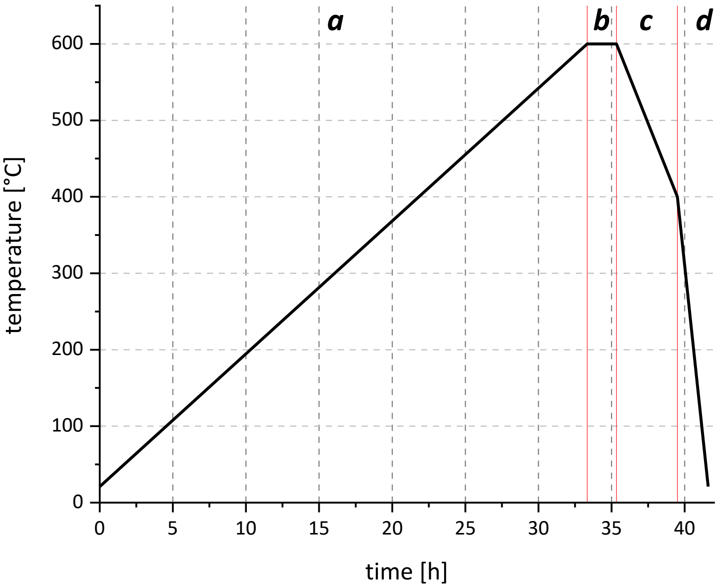

Fig. 7: *Temperature profile of the binder – burn – out process*

3.2.6. Sintering

For sintering the samples were placed on a planar crucible covered with coarse – grained tabular Al_2O_3 – powder to ensure unimpeded shrinkage and to avoid the attachment to the crucible. The sintering was performed in a high temperature furnace (Thermconcept GmbH, Bremen, Deutschland) with the following temperature profile, schematic in Fig. 8.:

(a) first heating rate of 10 °C/min to 1200 °C, (b) second heating rate of 5 °C/min to 1550 °C, (c) dwelling time of 2 h, (d) cooling rate of 5 °C/min to room temperature.

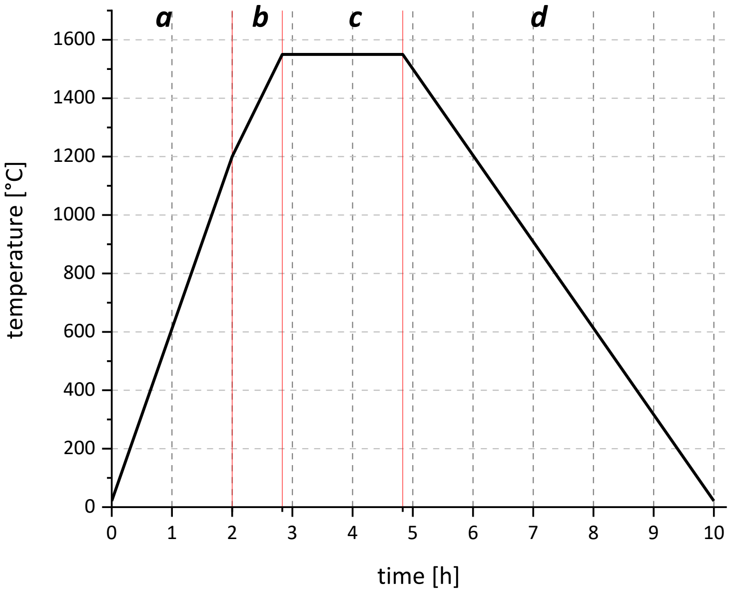

Fig. 8: *Temperature profile of the sintering – process*

3.3. Microstructural and Mechanical characterization

3.3.1. Sample preparation

After sintering the final dimensions (L×W×H) of the ceramic plates were ≈ 47 x 47 x 2.7 mm due to shrinkage. For testing the plates were cut into 4 mm wide prismatic bars. Further sample preparation steps according to the type of characterization will be described in detail in each chapter.

3.3.1.1 Grinding and Polishing

For the microstructural analysis as well as for the determination of the Vickers hardness, the side surfaces of the prismatic bars were grinded and polished stepwise to a mirror finish of 1 µm (see Table 2). Two samples of each composition were glued with wax on a circular plate and plan – parallel coarse grounded to a grid grade of 15 µm. For polishing a Struers Pedemax – 2 polishing machine (Struers Tech, DK2610 Copenhagen, Denmark) was used with a set of Struers MD-Plan™ and MDDur™ polishing cloths and corresponding diamond suspensions.

Table 2: *Steps of grinding and polishing*

step	grid grade [µm]	pressure level	time [min]
1	9	3	10
2	6	5	20
3	6	5	20
4	6	3	10
5	3	3	15
6	1	3	5

3.3.1.2 Thermal etching

For the microstructural characterization of the textured alumina samples, thermal etching was performed by using a HF generator (AHT Austria, Rottenmann, Austria) and an infrared radiation pyrometer (Dr. Georg Maurer GmbH, Kohlberg, Germany). The grinded and polished samples were thermally etched at 1400 °C for 20 minutes.

3.3.1.3 Notching of samples

The fracture toughness (K_{IC}) of the textured alumina samples was evaluated with the Single Edge V – Notched Beam method (SEVNB) after the standards of ISO 23146 [42]. A sharp defined V – notch was prepared using a similar construction as by NISHIDA et al [43]. The sample was notched by using a sharp razor blade and diamond pastes with two different particle sizes, 6 µm and 1 µm. Starting with the 6 µm paste for inducing a coarse notch, followed by a sharpening with the 1 µm grained paste. In accordance to the norm, the depth has to be 20-30 % of the height of the sample and the notch – root radius must be smaller than the grainsize of the sample. Considering the height of the fabricated samples (≈ 2.7 mm) the length and the radius of the notch was approximately 600-800 µm and < 10 µm, respectively.

3.3.1.4 Chamfering of samples

For the determination of the mechanical strength prismatic bars were tested via 4 – point bending according to the standards of EN 843-1 [44]. To avoid the effect of induced defects during machining, the edges of the surface loaded under tension during testing were chamfered with 0.5 x 0.5 mm and an angle of 45°.

3.3.2. Microstructure characterization

3.3.2.1 Optical Light Microscope (LIMI)

For the optical images a light microscope (BX50 Olympus, Shinjuku, Tokio, Japan), an upright microscope (eclipse LV100ND, Nikon, China) with DS-Ri2 camera as well as the stereo microscope (SZH10 research stereo, Olympus, Shinjuku, Tokio, Japan) were utilized.

3.3.2.2 Scanning Electron Microscope (SEM)

The observation of the microstructure was made by using a scanning electron microscope (SEM, JEOL JCM-6000Plus Neoscope™, JEOL Ltd., Tokyo, Japan). To receive an electrical conductive surface, selected thermally etched samples were gold coated using an Agar Sputter Coater. For enhancing conductivity, a copper band was attached in addition onto the samples. Backscattered SEM images were also taken to perform phase analysis and to determine the actual content of second phase, by using the Olympus stream software. On the other side, using SEM images, the average grain size was measured of ≈ 350 elongated grains in horizontal and vertical direction by the linear intercept method. With the average grain size in horizontal and vertical direction the aspect ratio was determine for monolithic TA samples as well as for TA with various contents of m-ZrO_2.

3.3.2.3 Determination of the quality of texture

3.3.2.3.1 Degree of orientation: X-ray diffraction pattern

X-Ray diffraction (XRD, Bruker AXS D8 Advance, Germany) was utilized to determine the degree of orientation for monolithic TA and for each composition of TA with m-ZrO_2 as second phase. Due to alignment of templates during the tape casting process, the aim is that the basal surfaces (0001) of the textured grains are parallel to the sample surface. Determining the Lotgering Factor (LF), published in 1959 by F. K. Lotgering [45], information about the degree of orientation can be provided. A value of LF = 1 defines a perfect textured microstructure. For the evaluation of LF, X-Ray diffraction patterns from (i) textured and (ii) equiaxed alumina as reference are compared, applying the following equation (2):

$$LF = \frac{P_{(00l)} - P_0}{1 - P_0} \tag{2}$$

where $P_{(00l)}$ is the ratio of intensities for textured materials and P_0 for non – oriented material $P_{(00l)}$ and P_0 can be determined with the following equations (3) and (4):

$$P_{(00l)} = \frac{\sum I_{(00l)}}{\sum I_{(hkl)}} \; for\ textured \tag{3}$$

$$P_0 = \frac{\sum I_{0(00l)}}{\sum I_{0(hkl)}} \; for\ equiaxed \tag{4}$$

where $I_{(ool)}$ and $I_{0(ool)}$ are the intensities of the peaks representing the characteristic (0001) peaks; $I_{(hkl)}$ and $I_{0\,(hkl)}$ are the intensities of all peaks detected in the XRD pattern.

3.3.2.3.2 Distribution of orientation: X-ray Rocking Curve

For a more accurate characterization of texture, the quality of orientation was additionally determined by using the rocking curve method. This technique provides information about the degree and the volume fraction of oriented grains. By fitting the measured rocking curve with the March – Dollase equation (5) the fitting parameters r and f, describing the degree of grain orientation and the volume fraction of oriented grains respectively, can be determined:

$$F(f,r,\theta) = f(r^2cos^2\theta + \frac{sin^2\theta}{r})^{-\frac{3}{2}} + (1-f) \tag{5}$$

where f ($0 \leq f \leq 1$) is the volume fraction of the oriented material, r ($0 \leq r \leq 1$) the orientation parameter of the grains and θ the specimen tilt angle (the angle between the texture axis and the scattering vector). A small r – value indicates a narrow distribution of orientated platelets normal to the sample surface. For a perfectly textured system, r would be 0 and f = 1.

Additionally to the fitting parameters, the Full Width at Half Maximum (*FWHM*) of the fitted curve provides information about the texture. A narrow *FWHM* implies perfect oriented grains. [46]

3.3.3. Determination of physical properties

3.3.3.1 Density measurements

The density of the bulk materials was evaluated according to the Archimedes principle ÖNORM EN 623-2 [47]. The mass of three samples of each composition were measured in air (m_d) and liquid (m_l) with a Sartorius weight scale (Sartorius Basic Lite BL210s). The temperature of the distilled water used as liquid, was measured after each weighting in liquid to determine the corresponding density of the water (ρ_l).

The bulk density (ρ_b) was calculated by applying equation (6).

$$\rho_b[g/cm^3] = \frac{m_d * \rho_l}{m_l} \tag{6}$$

where m_d and m_l are the masses in [g] of the samples measured in air and in liquid .

To obtain the relative density (ρ_{rel}), the bulk density is devided by the theoretical density (ρ_{theor}) as given in equation (7):

$$\rho_{rel}[\%] = \frac{\rho_b}{\rho_{theor.}} * 100\ \% \tag{7}$$

3.3.3.2 Young's Modulus

The measurement of the Young's modulus (E) was accomplished only on the monolithic TA. Three samples were tested (i) parallel and (ii) perpendicular to the [0001] direction of the aligned grains, see Fig. 9.

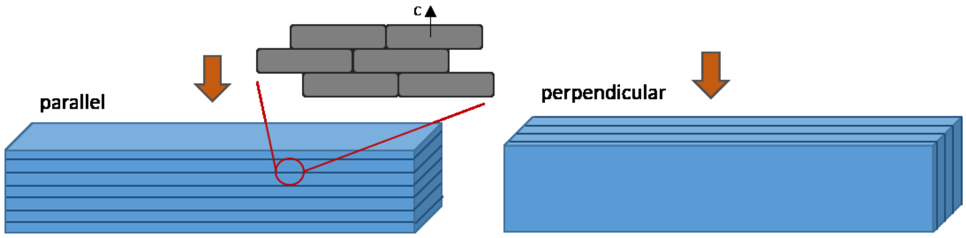

Fig. 9: *Schematic of testing orientation of TA samples for Young's Modulus measurements*

The determination was performed in accordance to the norm EN 843-2 [48] using a universal testing machine (Messphysik Microstrain, Messphysik Materials Testing GmbH, 8280 Fürstenfeld, Austria) with a 3 – point bending set – up (span 40 mm) and a 100 N load cell. At ambient conditions (T = 22.8 °C, RH = 28 %) an initial load of 2 N was applied, followed by three repeating loading and unloading cycles to a maximum load of 30 N with a displacement rate of 0.5 mm/min. The Young's modulus was determined with the following equation (8):

$$E = \frac{kS_1}{4BW^3} \tag{8}$$

where k is the slope [N/mm], S_1 is the bottom span of the testing assembly in [mm], B is the width of the sample in [mm] and W the height in [mm].

3.3.4. Determination of mechanical properties

3.3.4.1 Vickers Hardness

For the determination of the Vickers Hardness, indents with 10 kg were made perpendicular (see Fig. 10) to the (0001) planes of the oriented grains.

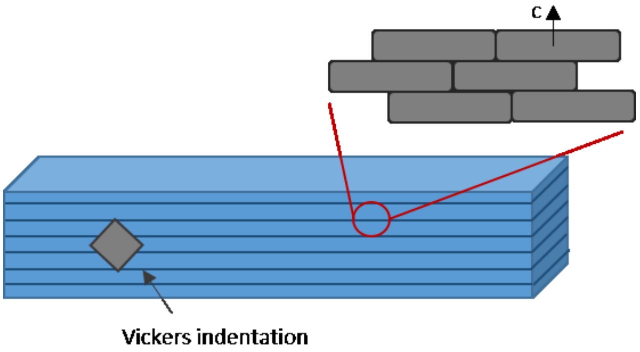

Fig. 10: *Schematic of testing orientation for TA at HV10 evaluation*

According to the standards EN 843-4 [49], a Zwick Indenter machine (Zwick 3212B GmbH&Co, 7900 Ulm, Germany) was utilized. With a mass of 10 kg and a penetration time of 10 s, ten intents in two samples for each formulation, were made. Afterwards, the diagonals were measured with a light microscope (BX50 Olympus, Shinjuku, Tokio, Japan) and HV10 evaluated according equation (9):

$$HV(F) = 1{,}8544\,\frac{F}{d^2} \tag{9}$$

where *F* is the applied load in [kg] and *d* represents the arithmetic average of the two diagonal impression lengths in [mm].

3.3.4.2 Fracture Toughness

The fracture toughness (K_{IC}) was evaluated with the Single Edge V – Notched Beam method (SEVNB) in a 4 – point bending set – up (span 40 – 20 mm) according to EN ISO 23146 [42]. For statistic validity, five samples of each composition were tested. Considering the monolithic textured alumina, samples were tested in two different directions: (i) parallel and (ii) perpendicular to the [0001] direction of the grains (Fig. 11). The composites, containing alumina and monoclinic zirconia, were only tested parallel to the [0001] direction.

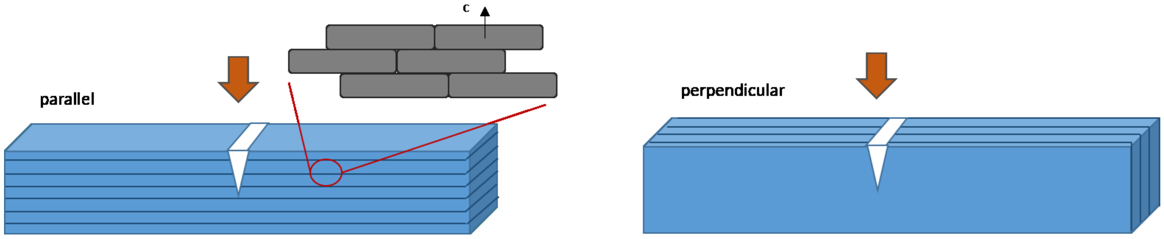

Fig. 11: *Schematic representation of testing orientation for TA at K_{IC} evaluation*

The testing was performed at ambient conditions (T = 23.6 °C, RH = 41 %) using a universal testing machine (Zwick Z010, Zwick GmbH &Co, 7900 Ulm, Germany) and the corresponding software, TestXpertII. The samples were placed with the V – notch on the side loaded under tension, a pre – load of 5 N was applied, followed by loading with a displacement rate of 0.5 mm/min until failure.

For the determination of the fracture toughness, the V – notch was measured on three different positions after fracture. The K_{IC} value was evaluated according to equation (10) following ISO 15732 [50].

$$K_{IC} = \frac{F}{B\sqrt{W}} \frac{S_{1-}S_2}{W} \cdot \frac{3\sqrt{a}}{2(1-a)^{3/2}} Y^* \tag{10}$$

where *F* is the maximum applied load, *B* is the width of the sample in [m], *W* is the height in [m], S_1 is the outer span of the testing assembly in [m], S_2 is the inner span in [m], *a* is the length of the V – notch in [m] and *Y** is the non – dimensional geometrical factor which is calculated for bar – shaped samples with the following equation (11):

$$Y^* = 1.9887 - 1.326a - \frac{(3.49 - 0.68a + 1.35a^2)a(1-a)}{(1+a)^2} \tag{11}$$

3.3.4.3 Mechanical strength

The mechanical strength was only evaluated for the monolithic TA with the 4 – point bending test (span 40 – 20 mm) following the standards of EN 843-1 [44]. For the procedure, a Zwick Z010 universal testing machine (Zwick GmbH &Co, 7900 Ulm, Germany) with the TestXpertII software was utilized. The testing, at ambient conditions (T = 21.7 °C, RH = 30 %), was performed by applying an initial load of 10 N, followed by a constant loading with a displacement rate of 1.5 mm/min until fracture. According to EN 843-1, the testing speed has to be adjusted so that the sample breaks within 5 – 15 s. For a statistically significant result, a set of 29 samples was tested. The bending strength σ_f in [MPa] was evaluated according to equation (12):

$$\sigma_f = \frac{3F(S_1 - S_2)}{BW^2} \tag{12}$$

where F is the maximum applied load at break in [N], B is the width of the sample in [mm], W is the height in [mm], S_1 is the outer span of the testing assembly in [mm], S_2 is the inner span in [mm].

4. Results and Discussion

In this section, first the results of the characterization of monolithic textured alumina (TA) according to microstructural, physical and mechanical properties will be discussed. Second, the measured values, as relative density, fracture toughness or Vickers hardness for textured alumina, with additions of different contents of monoclinic zirconia (0.5 – 20 vol%) will be compared.

4.1. Characterization of monolithic textured alumina

4.1.1. Microstructural characteristics

Fig. 12 a) shows an SEM image of the microstructure of a monolithic textured alumina (TA) sample. The elongated oriented grains were measured having an average grain size of 8.94 ± 6.12 µm in horizontal and 2.26 ± 1.16 µm in vertical direction, respectively. Thus, resulting in an aspect ratio of ≈ 4.0. Considering the quality of texture of the microstructure it can be observed that the manufactured samples had layers of highly and rather irregular oriented grains, see Fig. 12 b) and c). In some cases, regions of irregularities could be observed, which might be a result from the manufacturing process e.g. due to different vaporization speeds of the solvents at different positions of the tape.

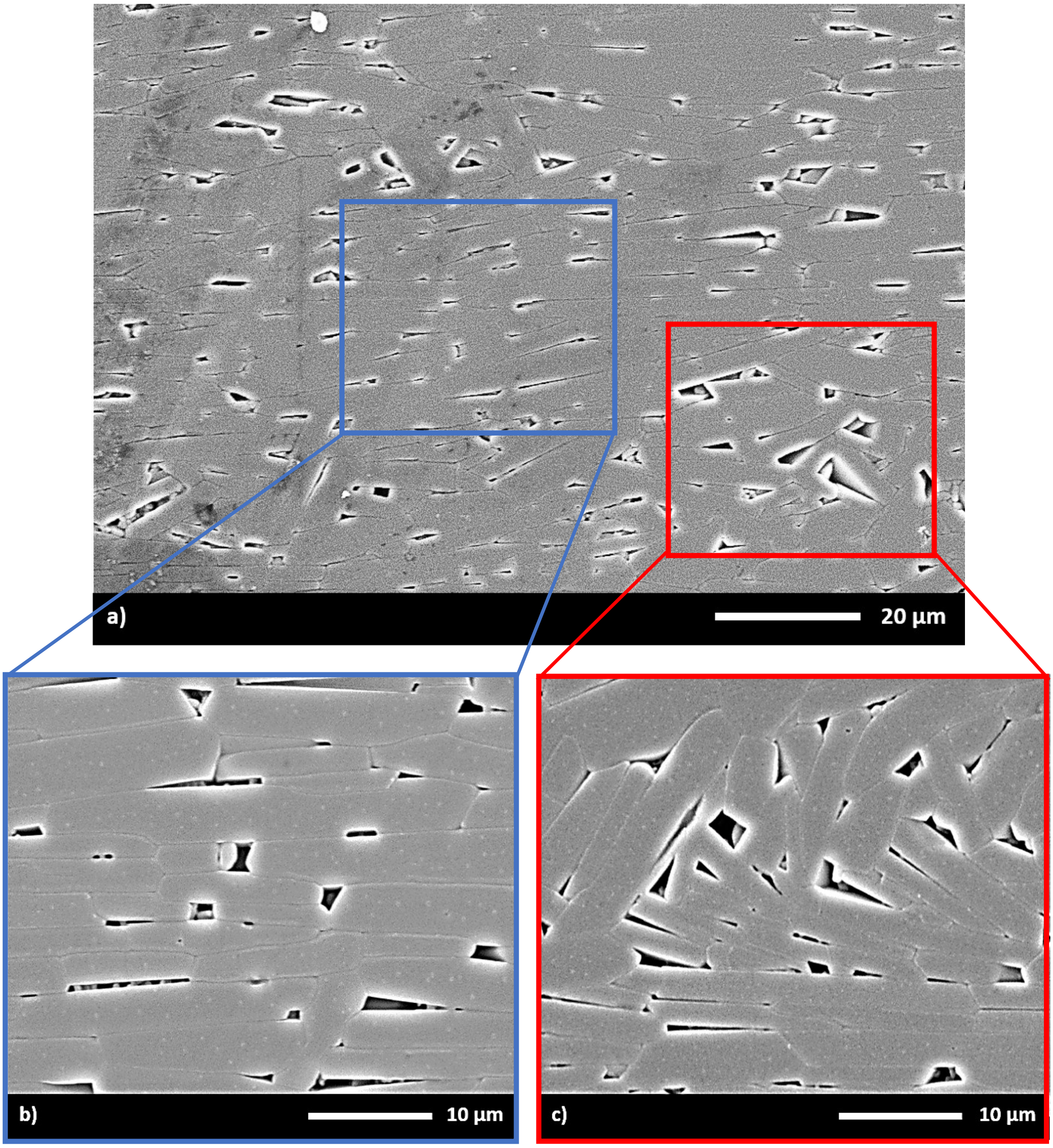

Fig. 12: *a) SEM micrograph showing the microstructure of TA, in detail regions with b) highly oriented grians and c) irregular oriented grains*

To quantitatively describe the quality of texture in TA the Lotgering factor (LF) was determined from XRD patterns of equiaxed and textured alumina. Fig. 13 a) and b) display the XRD pattern measured from a textured alumina and an equiaxed alumina sample, respectively. Comparing the patterns of textured and equiaxed alumina, the peaks for the (0006) and (00012) planes are dominant for TA, indicating oriented grains. The LF for textured alumina was evaluated to be 0.42. This result is relatively low compared to the a desired value of > 0.90, already measured for TA as found in literature [15]. The rather low measured LF for TA might be attributed to the described irregular regions of oriented grains. Since the penetration depth of X-rays in alumina was estimated to be in the range of 20-30 µm, a layer with irregularities might have been measured.

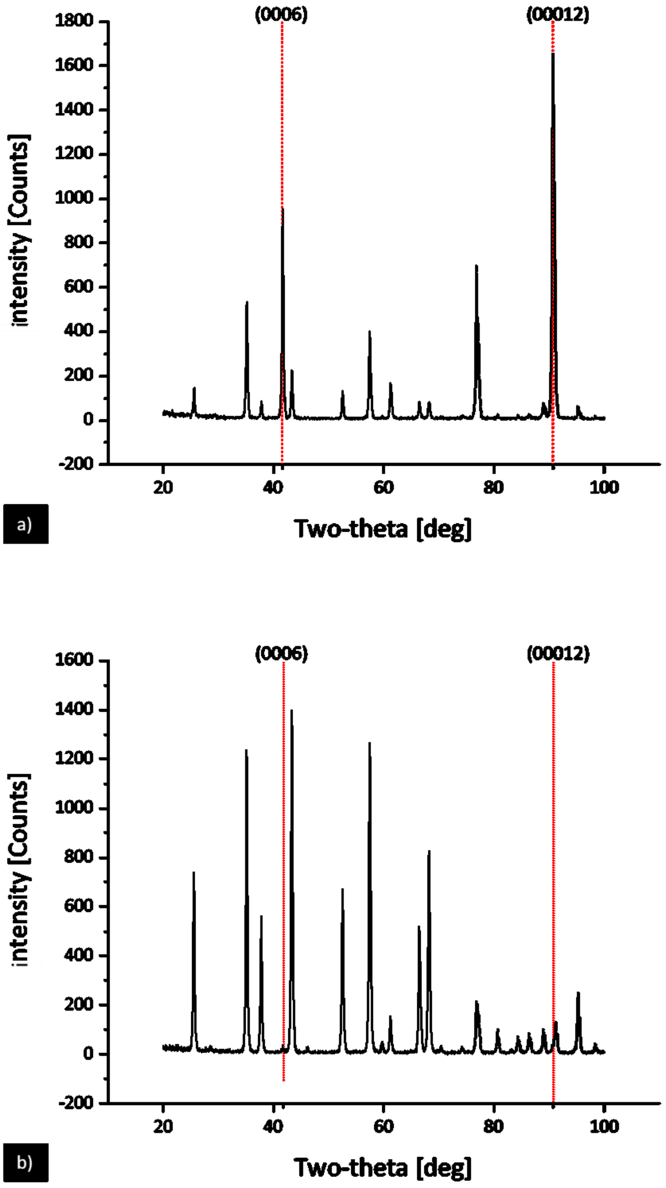

Fig. 13: *XRD patterns of a) textured and b) randomly oriented alumina*

Additionally, the Full Width of Half Maximum (FWHM) (Fig. 14) and the fitting parameters r and f from the March – Dollase equation from a X-ray rocking curve were determined to describe the quality of texture in more detail. The determined FWHM was 10.2 °, r = 0.24 and f = 0.66 for textured alumina, respectively. The lowest FWHM and r – value found in literature for textured alumina so far was 4.6 ° and 0.13 respectively [27].

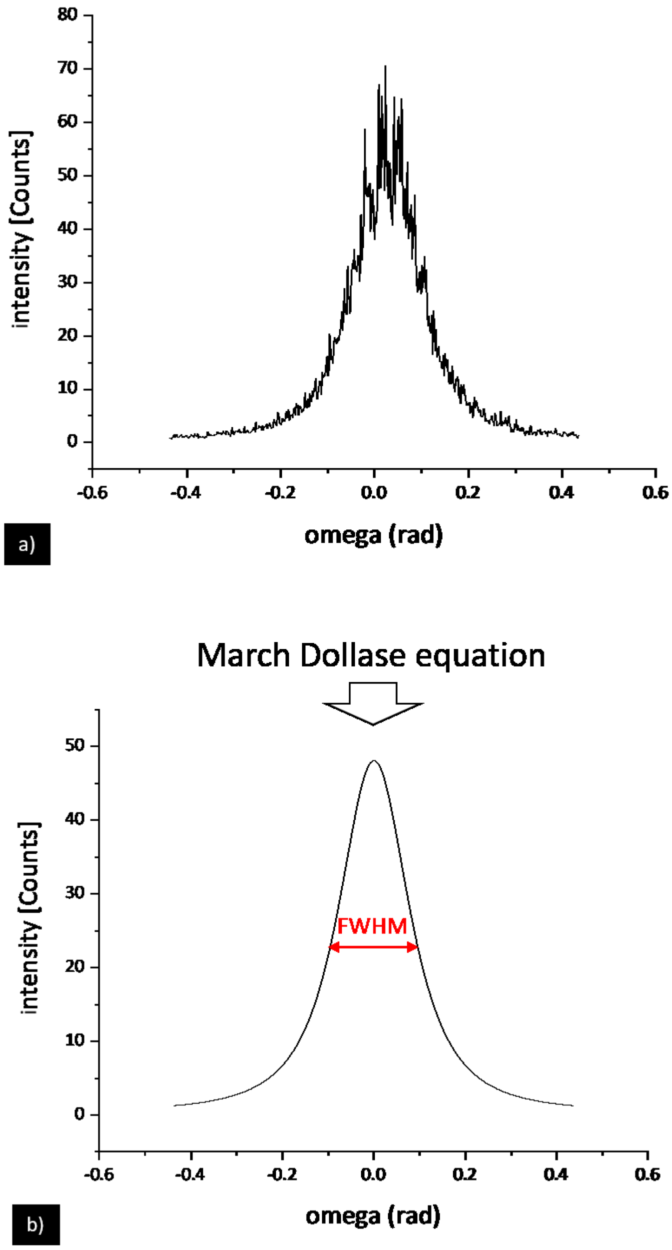

Fig. 14: a) Rocking curve measured for TA and b) the corresponding March – Dollase fit

4.1.2. Physical properties evaluation

4.1.2.1 Density

The bulk density (ρ_b) of the fabricated TA samples, measured via the principle of Archimedes, was 3.8031 ± 0.0069 g/cm^3. Using the theoretical density of alumina, ρ_{th}=3.9860 g/cm^3 [1] a relative density (ρ_{rel}) of 95.4 % was evaluated. The lower density in textured microstructures can be attributed to the anisotropic grain growth, leading to a reduction of pore closure [27,51].

4.1.2.2 Young's Modulus

The Young's modulus (E) was measured (i) parallel ($E_{//}$) as well as (ii) perpendicular ($E_{\perp}$) to the [0001] direction of the aligned grains (see Fig. 9).

The measured Young's moduli for both orientations of TA samples are listed in Table 3. For comparison, the Young's modulus of equiaxed alumina was estimated considering the dependence of the Young's modulus on density. Applying equation (13) [52] the porosity (P) of ≈ 5 % measured in TA samples, as well as a theoretical Young's modulus (E_0) [1] of 400 MPa for > 99 % dense alumina was taken.

$$\mathbf{E} = \mathbf{E_0}(1 - 1.9P + 0.9P^2) \tag{13}$$

Table 3*: Measured Young's moduli of TA for different testing orientations and the estimated theoretical value of equiaxed alumina*

$E_{||}$ [GPa]	$E_{\perp}$ [GPa]	E_{th} [52] [GPa]
370 ± 3	366 ± 2	363

The Young's moduli for the different measured directions ($E_{//}$ and $E_{\perp}$) of TA are statistically comparable and in the same range of the calculated theoretical value for a monolithic EA alumina with a comparable porosity of ≈ 5%.

4.1.3. Mechanical properties

4.1.3.1 Vickers Hardness

The Vickers hardness was determined perpendicular to the (0001) planes of the oriented grains (Fig. 10), since the imprints parallel to the basal planes of textured alumina are not valid for hardness measurements due to a non – defined shape of the indents. This can be related to occurring sliding effects of the tailored grains, where the applied load does not cause inelastic deformation but rather delamination of the templates. In comparison, perpendicular to the basal planes, well – defined, valid imprints for the evaluation of HV10 can be made (see Fig. 15). Contrary to what it would be expected in brittle materials, the cracks are not propagating from the corners, they rather emanate from the edges. This might be a result of the anisotropy and the morphology of the textured grains. The evaluated Vickers hardness, based on the imprints perpendicular to the (0001) planes for TA is HV10 = 12.5 ± 0.5 GPa. This value is significantly lower than for monolithic equiaxed alumina as found in literature: HV10 ≈ 19 GPa [39]. On the one hand, this might be due to a higher porosity found in TA and relatively larger grains. On the other hand, as described in literature, the properties of an alumina single crystal are anisotropic. The basal plane of the hexagonal lattice has the highest value in comparison to the prismatic planes. However, since the imprints for a valid determination of the Vickers hardness were made parallel to the prismatic planes, a lower hardness is measured [53,54].

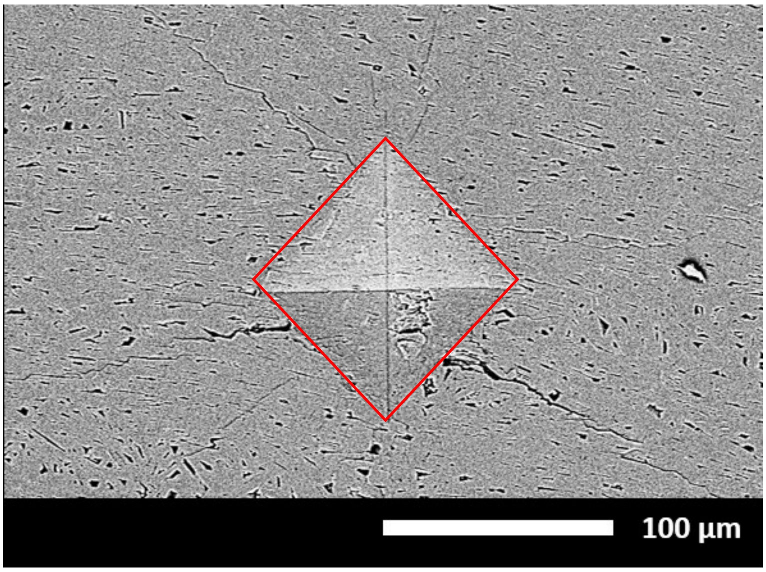

Fig. 15: *SEM micrograph of Vickers indentations imprint of textured alumina*

4.1.3.2 Fracture Toughness

The fracture toughness was evaluated (i) parallel ($K_{IC\,//}$) and (ii) perpendicular ($K_{IC\,\perp}$) to the basal plane of the aligned grains (see Fig. 11).

The measured fracture toughness (K_{IC}) of TA for different testing orientations as well as the K_{IC} values of an alumina single – crystal (tested in [0001] direction) [55] and for equiaxed alumina are listed in Table 4.

Table 4: *Fracture toughness of TA and single – crystal alumina*

$K_{IC\,\|\|}$ [MPa m$^{1/2}$]	$K_{IC\,\perp}$ [MPa m$^{1/2}$]	$K_{IC\_[0001]}$ [55] [MPa m$^{1/2}$]	K_{IC_EA} [29] [MPa m$^{1/2}$]
5.40 ± 0.21	4.14 ± 0.15	4.54 ± 0.21	3.0 – 4.0

Comparing the measured K_{IC} values for TA samples in both directions, it can be observed that the fracture toughness measured parallel to the basal plane is significantly higher than measured perpendicular. This might be related to the anisotropic properties of an alumina single crystal. [53] Regarding $K_{IC\,\perp}$ the crack is hardly deflected and propagates straight through the bulk material. Whereas, in the case of $K_{IC\,//}$, as schematically drawn in Fig. 16 toughening mechanisms as crack deflection and bifurcation may take place.

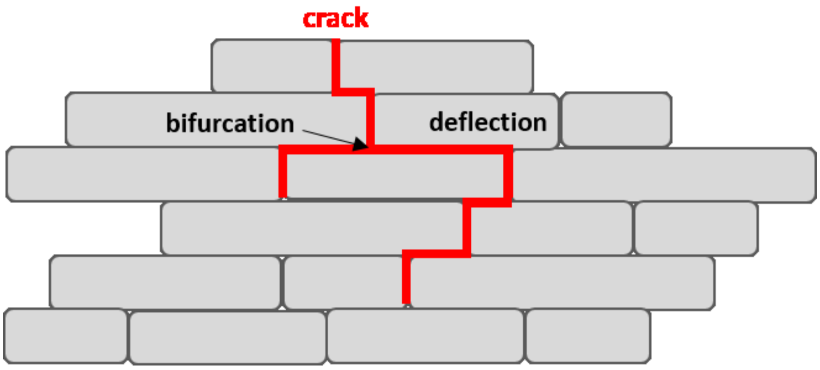

Fig. 16: *Schematic of toughening mechanisms in textured materials*

Regarding $K_{IC\,||}$ an even higher fracture toughness was measured than for the basal plane of an alumina single crystal ($K_{IC\_[0001]}$), which can be associated with the morphology of the textured microstructure. The values measured for TA in the different directions are both higher than the fracture toughness found for equiaxed alumina. Here, the grain orientation as well as the larger grain size of the textured structure in comparison to EA might be beneficial for increasing the fracture toughness in alumina.

Fig. 17 shows the crack path in a parallel tested TA sample, where the crack propagates intergranular along the grain boundaries and is deflected due to the morphology and crystallographic orientation of the textured grains.

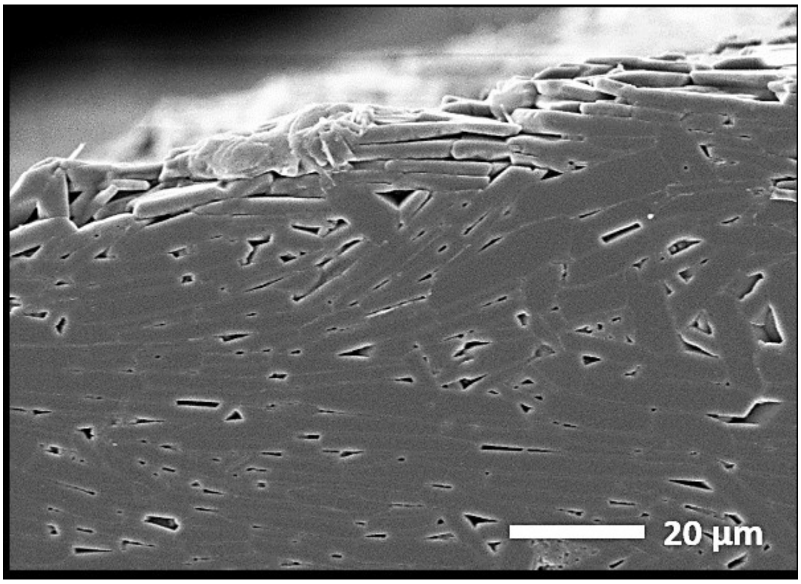

Fig. 17: *SEM micrograph of the fracture path of a TA sample*

To visualize crack initiation and propagation in textured microstructures, a crack was induced in a notched sample. Using a penetration medium, the pre – crack could be made visible on both sides of the TA sample. Fig. 18 shows light – microscopic images from a) the front – and b) the back – side of the TA sample. It must be highlighted that the crack paths on the different sides appear to be different. This might be described as a result of the textured grain structure, where mechanisms as crack deflection and bifurcation lead to an anisotropic 3 dimensional crack propagation, with corresponding increase in fracture resistance of the material.

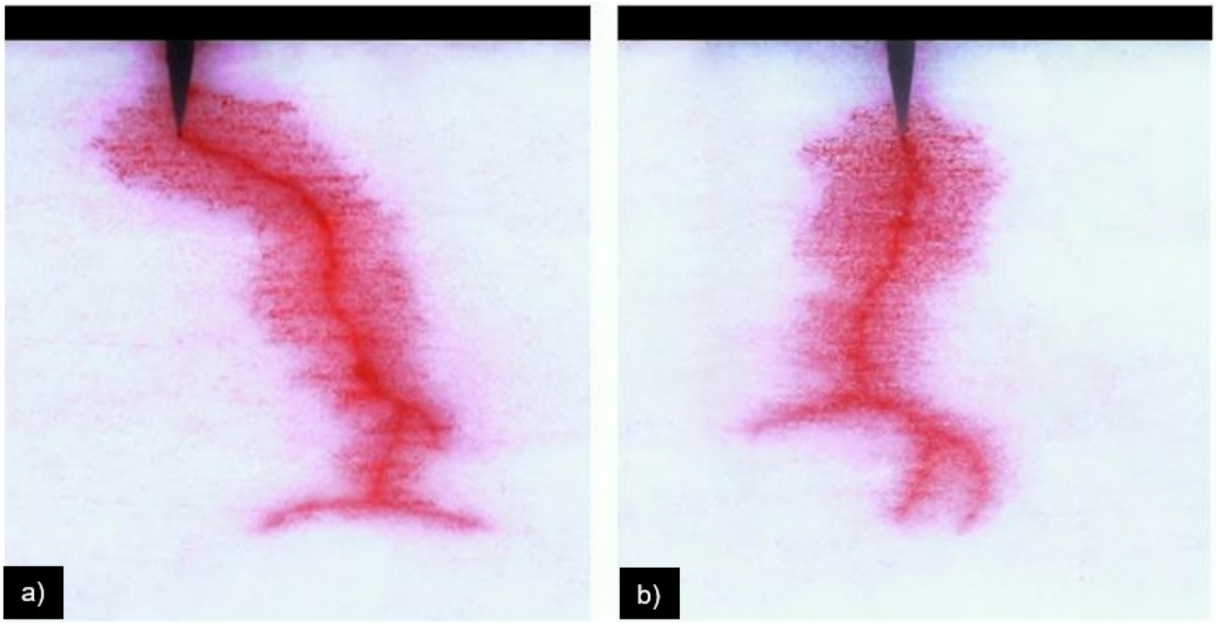

Fig. 18: *Optical light micrograph showing the crack propagation of TA: a) front – side and b) back – side*

4.1.3.3 Mechanical strength

The bending strength for TA was evaluated on 29 samples via 4 – point bending and is plotted in a Weibull diagram, in Fig. 19. The characteristic strength (σ_0) and the Weibull modulus (m) were evaluated according to Weibull statistics.

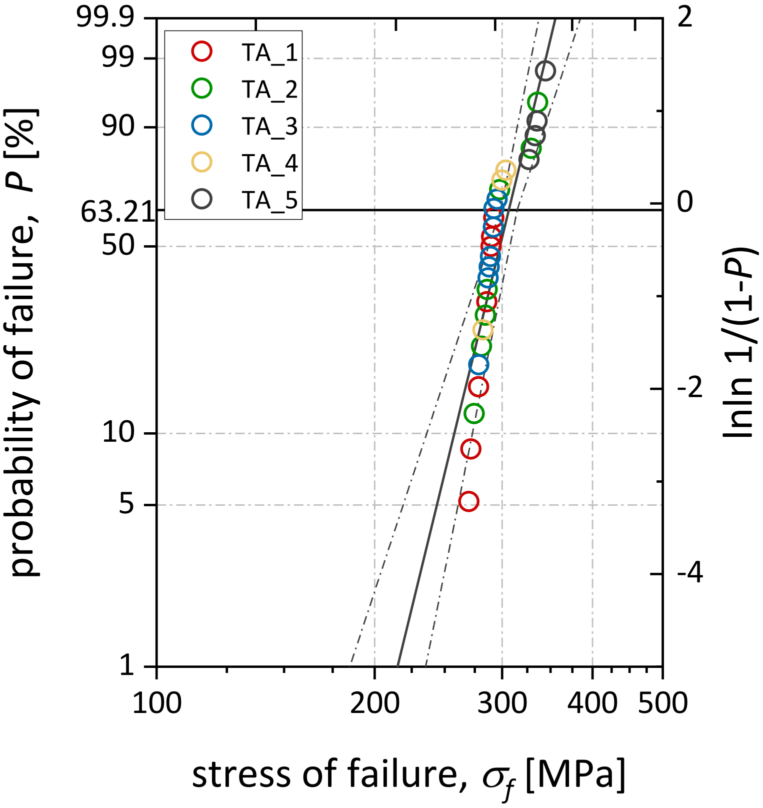

Fig. 19: *Weibull distribution of TA specimens tested under 4 – PB. The different colors represent different batches.*

The probability of failure (*P*) in [%] was determined according to equation (14) [56,57]:

$$P(\sigma) = 1 - exp\left[-\left(\frac{\sigma}{\sigma_0}\right)^m\right] \tag{14}$$

where σ is the applied stress in [MPa], σ_0 is the characteristic strength in [MPa] and m represents the Weibull modulus.

The characteristic strength σ_0 and the Weibull modulus m were evaluated via the Maximum Likelihood – Method and can be determined according to the following equation (15): [58]

$$ln ln \frac{1}{1-P} = m\, ln \frac{\sigma}{\sigma_0} = m\, ln\, \sigma - m\, ln\, \sigma_0 \tag{15}$$

The Weibull modulus m is find as the slope in the Weibull plot and σ_0 is determined via the point of intersection at P = 63.21%. The evaluated characteristic strength for TA is σ_0 = 306 ± 8 MPa [298 MPa – 315 MPa] with a Weibull modulus of m = 13 [9.6 – 15.8]. In comparison, as found in literature, the bending strength of equiaxed alumina ranges from 230 – 580 MPa with a Weibull modulus of 10 – 15 [1].

The relatively low characteristic strength of TA might be a result of the rather large grain size (approx. 9 ± 6 µm) and the occurring porosity due to texture of ≈ 4 – 5 %. However, considering the Weibull modulus of TA, it is rather high compared to equiaxed alumina. The larger grain sizes and higher apparent porosity in TA might appear as homogenously distributed defects of a similar size, resulting in a relatively high Weibull modulus. The low deviation of the measured bending strength values demonstrates a stable processing route for the fabrication of bulk materials with a homogeneous distribution of defects.

4.1.3.3.1 Fractography

Fig. 20 shows selected fracture surfaces of 4 – point bending tested TA samples. At the majority of analyzed samples, no significant defects could be indicated as fracture origin. Some samples showed regions of exaggerated grown grains, which might have led to failure. In general, the fracture surface of the TA samples appears to be rough and unplanar, which may be attributed to anisotropic crack propagation due to the textured microstructure.

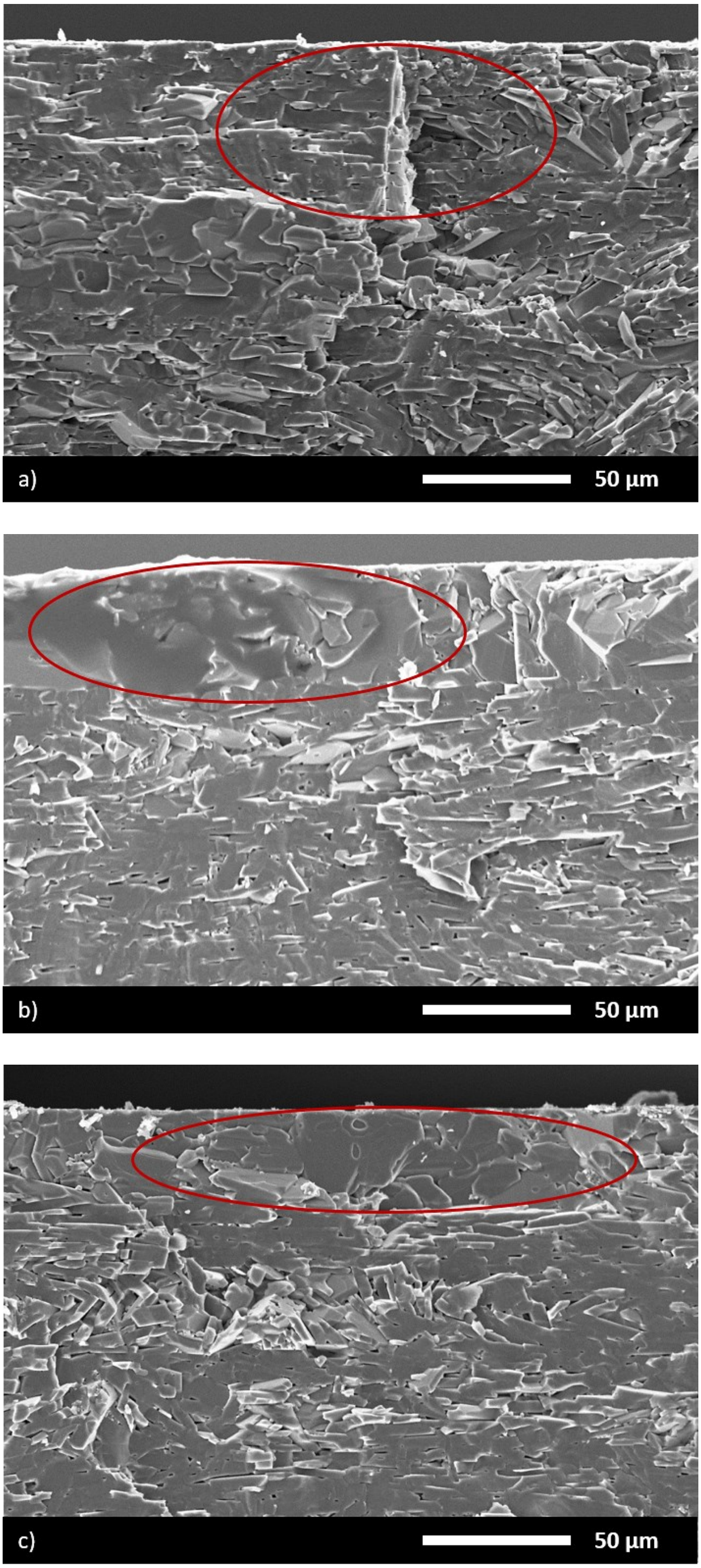

Fig. 20: *SEM micrographs showing selected fracture surfaces of TA samples*

4.2. Characterization of textured alumina doped with monoclinic zirconia

4.2.1. Microstructural characteristics

4.2.1.1 Scanning Electron Microscope (SEM)

Fig. 21 shows backscattered SEM images of the microstructure, where the dark material represents the alumina and the brighter phase monoclinic zirconia (m-ZrO_2) as second phase ranging from a) 0.5 vol% to f) 20.0 vol%. For the lowest content of m-ZrO_2 (0.5 vol% and 1 vol%), it might be observed that the second phase is rather distributed within the textured grains. However, with increasing second phase content, the monoclinic zirconia is rather distributed along the grain boundaries.

Furthermore, it can be observed that with increasing volume fraction of zirconia, the development of texture decreases. This can be related to the prohibition of grain growth due to the second phase. Here, the aspect ratio of the textured grains was determined, resulting in a decrease from a value of 3.68 for 0.5 vol%, 3.40 for 1 vol%, 3.35 for 2 vol % and 2.52 for 5 vol% m-ZrO_2, respectively (see Fig. 22).

Elongated aligned grains, defining a textured microstructure can be found until 2.0 vol% of second phase (Fig. 21 a) – c)). As well as the monolithic TA samples, also m-ZrO_2 doped alumina samples had alternating layers of highly textured and rather irregular oriented grains caused by the fabrication process. For the sample with 5 vol% m-ZrO_2 (see Fig. 21 d)) still some textured grains can be observed, but also regions of small, fine grained alumina occur. For the samples with 10 vol% and 20 vol% of m-ZrO_2 hardly grain growth of the templates occurred, resulting in a composite structure of spherical alumina and monoclinic zirconia grains with alumina templates.

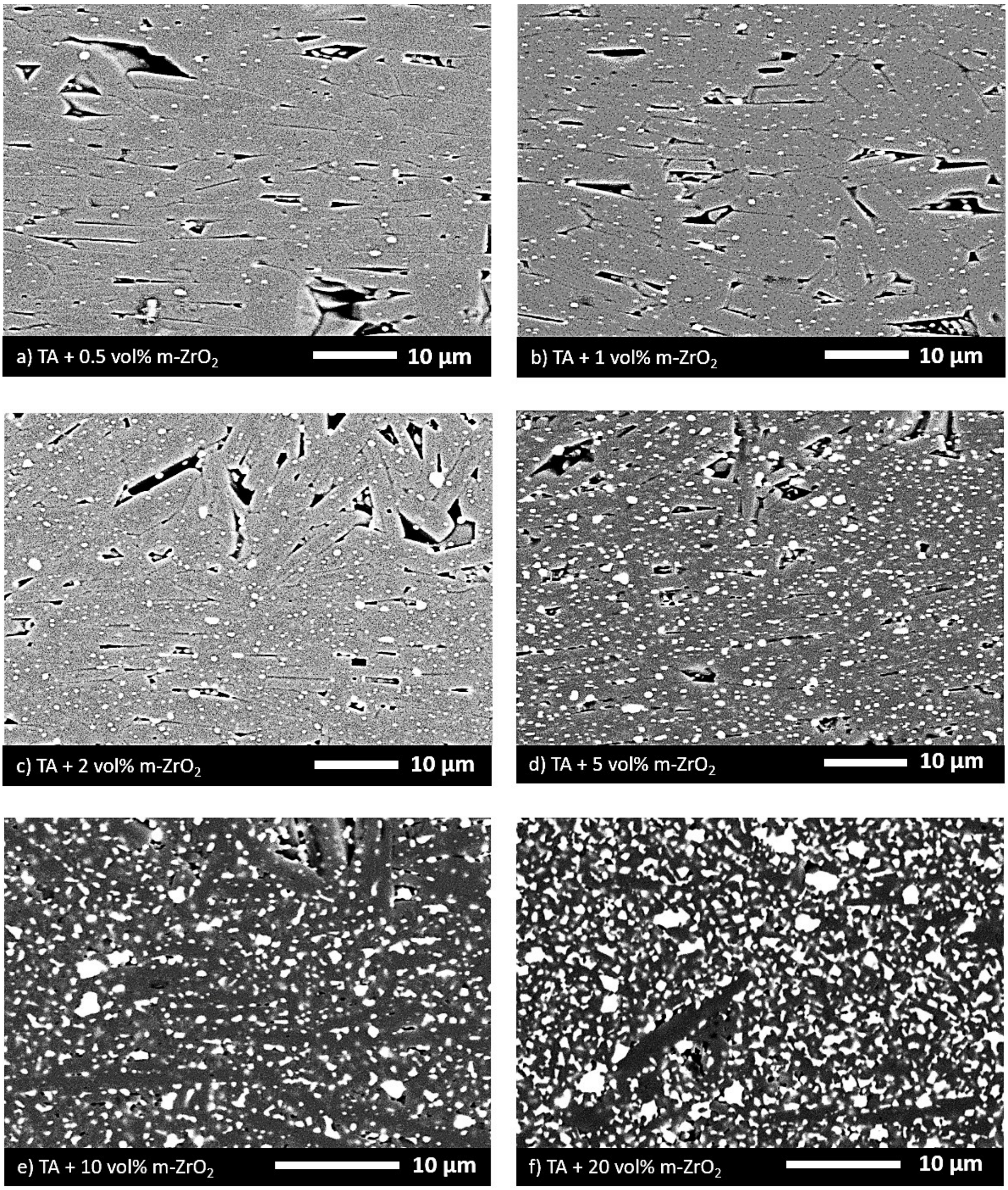

Fig. 21: *SEM micrographs by using BSD showing the microstructure of TA + increasing volume fraction of zirconia (a) 0.5 vol% m-ZrO$_2$ – f) 20 vol% m-ZrO$_2$)*

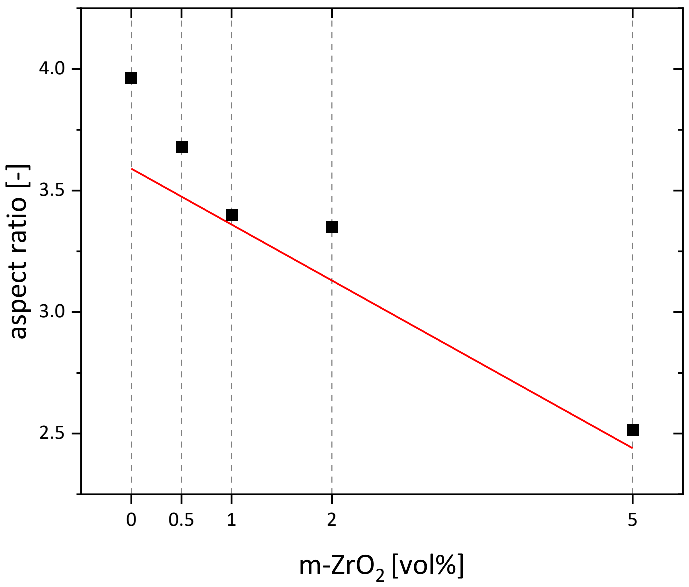

Fig. 22: *Comparison of aspect ratio from TA and its composites*

Additionally, the volume fraction of monoclinic zirconia in the fabricated samples was determined with phase analysis of the SEM images from Fig. 21. Table 5 shows the theoretical and evaluated volume fraction of added m-ZrO_2. All values are within the standard deviation, validating a stable and precise sample fabrication protocol.

Table 5: *Theoretical and experimental volume fraction of zirconia*

vol% m-ZrO_2 **th**	vol% m-ZrO_2 **exp**
0.5	0.4 ± 0.1
1.0	1.1 ± 0.1
2.0	2.0 ± 0.2
5.0	5.3 ± 0.4
10.0	10.1 ± 0.7
20.0	19.7 ± 1.2

4.2.1.2 Determination of the quality of texture

As illustrated with the SEM images (see Fig. 21), with increasing volume fraction of second phase the development of texture decreases. To quantify this effect, the Lotgering factor (LF) from XRD patterns as well as the Full Width of Half Maximum (FWHM) and fitting parameters of a XRD Rocking curve were determined.

4.2.1.2.1 Lotgering Factor (*LF*)

To determine the quality of texture the Lotgering Factor was evaluated by comparing the measured XRD patterns of all materials of study with equiaxed alumina as described for TA (see Fig. 13). Fig. 23 displays the evaluated LF values for the fabricated TA samples with various volume fractions of m-ZrO_2. It would have been expected that LF decreases with increasing m-ZrO_2 because of prohibition of templated grain growth due to a second phase. However, it can be noticed that the sample with 2 vol% m-ZrO_2 has the highest Lotgering Factor, even higher than the monolithic TA. This result, as for monolithic TA, might be related to inhomogeneities in the samples due to processing. As described, considering micrographs of the fabricated samples (Fig. 12 c)), alternating layers of highly textured and irregular oriented grains could be observed. As mentioned above the penetration depth of X-rays into alumina was estimated to be in the range of 20-30 µm. Therefore, if the with XRD analyzed surface had a structure of irregular oriented grains, a lower LF could be measured.

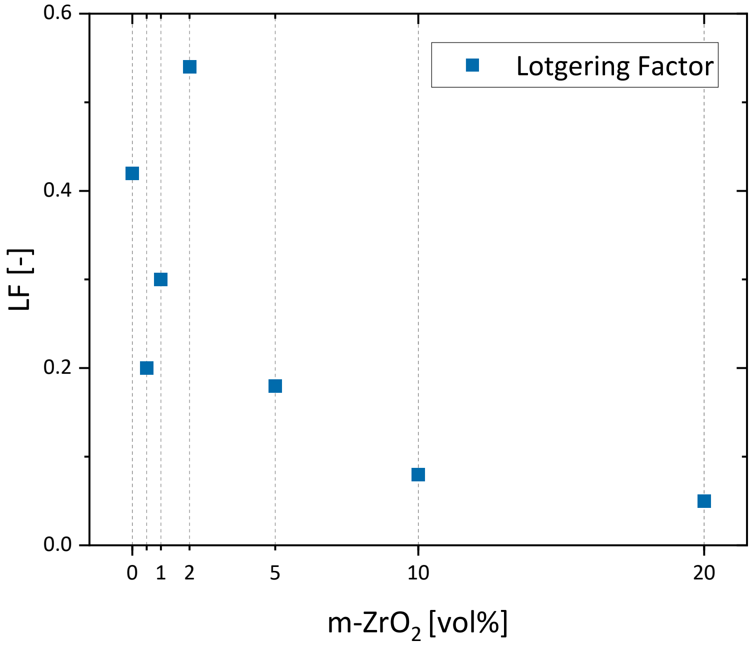

Fig. 23: *Comparison of LF – values for different volume fractions of m-ZrO_2 in alumina*

However, considering the diagram in Fig. 23, a tendency that the texture in TA decreases with increasing volume fraction of m-ZrO_2 can be estimated with the evaluated LFs. It can be stated that the samples with a m-ZrO_2 content lower than 10 vol%, the LFs are higher or approximately 0.2, which is related to a developed texture. In comparison for the contents of 10 vol% and 20 vol% the LF – values are below 0.1, which might be attributed to no texture, confirming the results of the analyzed micrographs (see Fig. 21).

4.2.1.2.2 Rocking Curve Method

As well as for monolithic TA, the Full Width of Half Maximum (FWHM) and the fitting parameters r and f from the March – Dollase equation from a X-ray rocking curve were additionally determined to describe the quality of texture in more detail. The results of the evaluated FWHMs as well as the fitted r – and f – values are listed in Table 6. For visualization, the r – and f – values evaluated for the various volume fractions of m-ZrO_2 in TA are plotted in Fig. 24.

Table 6: Results of Rocking Curve – measurement: FWHM, r – and f – values

materials	FWHM [°]	r – value [-]	f – value [-]
TA	10.2	0.24	0.66
TA + 0.5 vol% m-ZrO_2	11.5	0.26	0.47
TA + 1.0 vol% m-ZrO_2	10.2	0.24	0.47
TA + 2.0 vol% m-ZrO_2	7.3	0.19	0.48
TA + 5.0 vol% m-ZrO_2	10.2	0.24	0.31
TA + 10.0 vol% m-ZrO_2	9.6	0.23	0.09
TA + 20.0 vol% m-ZrO_2	12.7	0.28	0.03

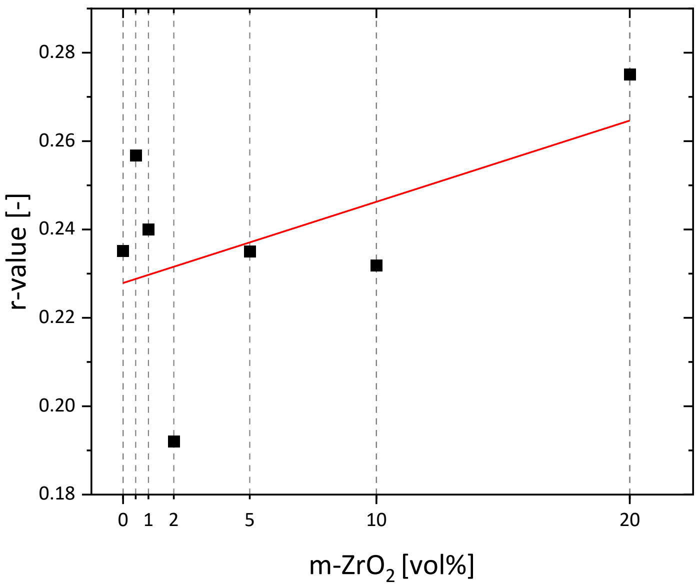

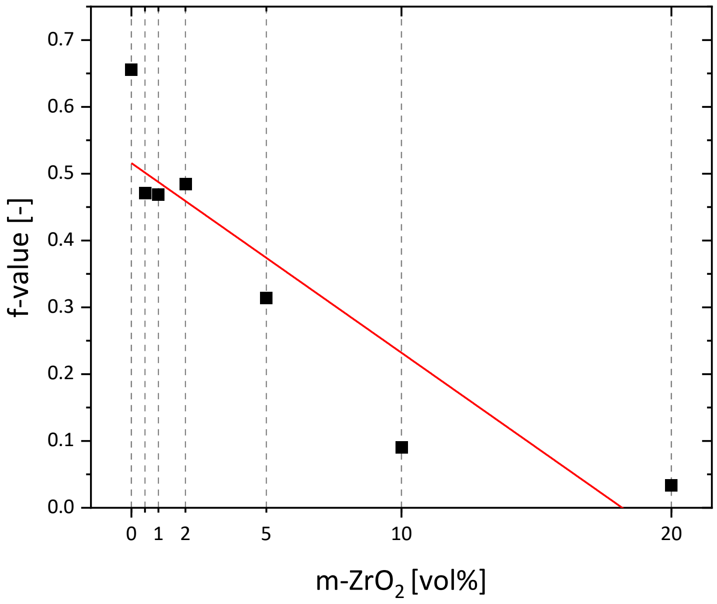

Fig. 24: *Comparison of r – and f – values with fitted trend line*

Comparable to the LF, the sample with 2 vol% m-ZrO_2 shows the highest degree of texture according to the evaluated FWHM of ≈ 7.3 ° and r – value (orientation parameter) of ≈ 0.19. Considering the f – value (textured volume fraction), TA achieves the highest value of ≈ 0.66. For the samples with contents of m-ZrO_2 from 0.5 vol% to 2.0 vol% have similar f – values of ≈ 0.47. This stability in f – values can be described with the distribution of grain size and shape. Micrographs and the determination of particle size showed that until a volume fraction of 2 vol% m-ZrO_2 in TA, the majority of the grains exhibit an elongated shape with an aspect ratio > 3.35. In comparison, for samples with m-ZrO_2 contents ≥ 5 vol%, the f – value decreases to 0.03 for 20 vol% m-ZrO_2. The decrease might be attributed to the appearance of a bi – modal grain shape and size distribution. Besides the textured grains also small spherical, equiaxed alumina and zirconia grains are present, reducing the volume fraction of textured grains. As shown in the micrographs (Fig. 21) the fraction of equiaxed grains increases with increasing m-ZrO_2 volume fraction, resulting in a decrease of the f – value. In general, as plotted in Fig. 24, the r – value increases and the f – value decreases with increasing volume fraction of second phase, describing a reduction of texture.

It can be noted, that the determination of texture by using the LF and Rocking Curve – method might not give representative information about the bulk properties. The estimated penetration depth of X-rays in alumina are approx. 20-30 µm. Inhomogeneities of randomly oriented grains that might occur at the measured surface of the textured samples can lead to values describing a lower degree of texture. Although, with the determination of LF, FWHM, r – and f – value, tendencies how the second phase of m-ZrO_2 affects the degree of texture in TA can be provided. Based on evaluated values using XRD measurements, it can be confirmed that TA with a volume fraction of monoclinic zirconia $\geq$ 5.0 vol% results in a significant reduction of texture in TA.

4.2.2. Physical properties

4.2.2.1 Density

Table 7 shows the evaluated bulk density, the estimated theoretical density and the relative density for each composition of TA and m-ZrO_2. The theoretical density was estimated according to the ratio of Al_2O_3 (ρ_{th} = 3.986 g/cm^3) to m-ZrO_2 (ρ_{th} = 5.830 g/cm^3) [1]. The standard deviation of the bulk density is relatively low, meaning there is no significant variation within a batch of manufactured samples. The increasing bulk density with increasing volume fraction of second phase is caused by the higher density of zirconia in comparison to alumina. With the addition of increasing contents of m-ZrO_2, the estimated theoretical and measured bulk density increases. Considering the relative density, a porosity of 3-5 % were evaluated especially in TA compositions containing zero or small contents of m-ZrO_2 (0-2 vol%). As already mentioned for monolithic TA, the high porosity (≈ 5 %) is discussed to be a result from anisotropic grain growth, leading to still open pores in the microstructure.

Table 7: *Evaluated bulk density, theoretical density and relative density for TA + 0 – 20 vol% m-ZrO_2*

materials	ρ_b [g/cm^3]	ρ_{th} [g/cm^3]	ρ_{rel} [%]
TA	3.8031 ± 0.0069	3.9860	95.41
TA + 0.5 vol% m-ZrO_2	3.8528 ± 0.0037	3.9952	96.44
TA + 1.0 vol% m-ZrO_2	3.8627 ± 0.0085	4.0044	96.47
TA + 2.0 vol% m-ZrO_2	3.8959 ± 0.0044	4.0229	96.84
TA + 5.0 vol% m-ZrO_2	3.9835 ± 0.0051	4.0782	97.68
TA + 10.0 vol% m-ZrO_2	4.0997 ± 0.0043	4.1704	98.32
TA + 20.0 vol% m-ZrO_2	4.2838 ± 0.0108	4.3548	98.36

In Fig. 25 the relative density is plotted for all materials of study. The increasing relative density with increasing second phase might be a result of the reduction of templated anisotropic grain growth during sintering. Whereas the growth of templates is reduced due to the second phase, a development of smaller, equiaxed grains occurs. As a result, the bulk material exhibits a closer packed microstructure. It might be highlighted that the relative density for TA samples with 10 vol% and 20 vol% m-ZrO_2 is similar (≈ 98%). This can be attributed to the majority of present equiaxed alumina and zirconia grains in comparison to elongated textured grains.

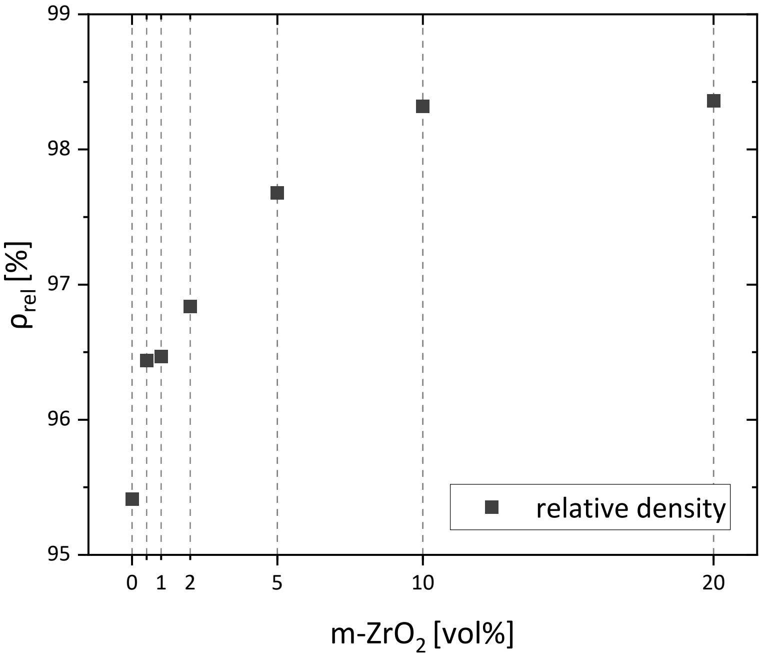

Fig. 25: *Comparison relative density for TA and its composites*

4.2.3. Mechanical properties

4.2.3.1 Vickers Hardness

As for the monolithic TA, for the evaluation of the hardness, indents with 10 kg were made perpendicular (see Fig. 10) to the (0001) planes of the elongated grains. The evaluated Vickers hardness for all materials of study, based on the imprints, are listed in Table 8.

Table 8: *Vickers hardness for TA + 0 – 20 vol% m-ZrO$_2$*

materials	**HV10** [GPa]
TA	12.5 ± 0.5
TA + 0.5 vol% m-ZrO$_2$	13.5 ± 0.4
TA + 1.0 vol% m-ZrO$_2$	13.5 ± 0.3
TA + 2.0 vol% m-ZrO$_2$	14.2 ± 0.4
TA + 5.0 vol% m-ZrO$_2$	14.7 ± 0.3
TA + 10.0 vol% m-ZrO$_2$	15.7 ± 0.2
TA + 20.0 vol% m-ZrO$_2$	14.6 ± 0.2

For TA the determined hardness is HV10 = 12.5 ± 0.5 GPa ; as already mentioned this is significantly lower than for monolithic equiaxed alumina as found in literature: HV10 ≈ 19 GPa [39]. As displayed in Fig. 26 the hardness increases with increasing volume fraction of m-ZrO$_2$ until 10 vol%. Comparable to the Young's Modulus, a proportional relation of HV10 and the relative density could be observed, see Fig. 26 [59]. It was hypothesized that with induced residual stresses due to the second phase, the hardness value of TA can be increased and adjusted. As described above, for TA samples with a content of m-ZrO$_2$ ≤ 5 vol% a homogeneous textured microstructure is still present (LF btw. 0.2 to 0.6). Considering these samples, it can be demonstrated that with increasing relative density and induced residual stresses due to the second phase, an increase of hardness in TA can be achieved. According to the sample with a volume fraction of 10 vol%, the highest HV10 value was measured (15.7 GPa). However, here a composite microstructure of small equiaxed alumina and zirconia grains is present rather, than a textured microstructure (LF ≈ 0.1). The high value of HV10 might be related to the low relative porosity and the present equiaxed microstructure. In comparison for TA with 20 vol% m-ZrO_2, HV10 decreases again. This drop might be attributed to the increasing effect of the hardness of zirconia, which is significantly lower than for alumina; HV10 (m-ZrO_2) ≈ 7 GPa [41]. Based on these results it can be stated that a second phase in textured alumina allows to adjust the hardness. A continuous increase in hardness with increasing second phase can be observed until ≈ 10 vol% m-ZrO_2.

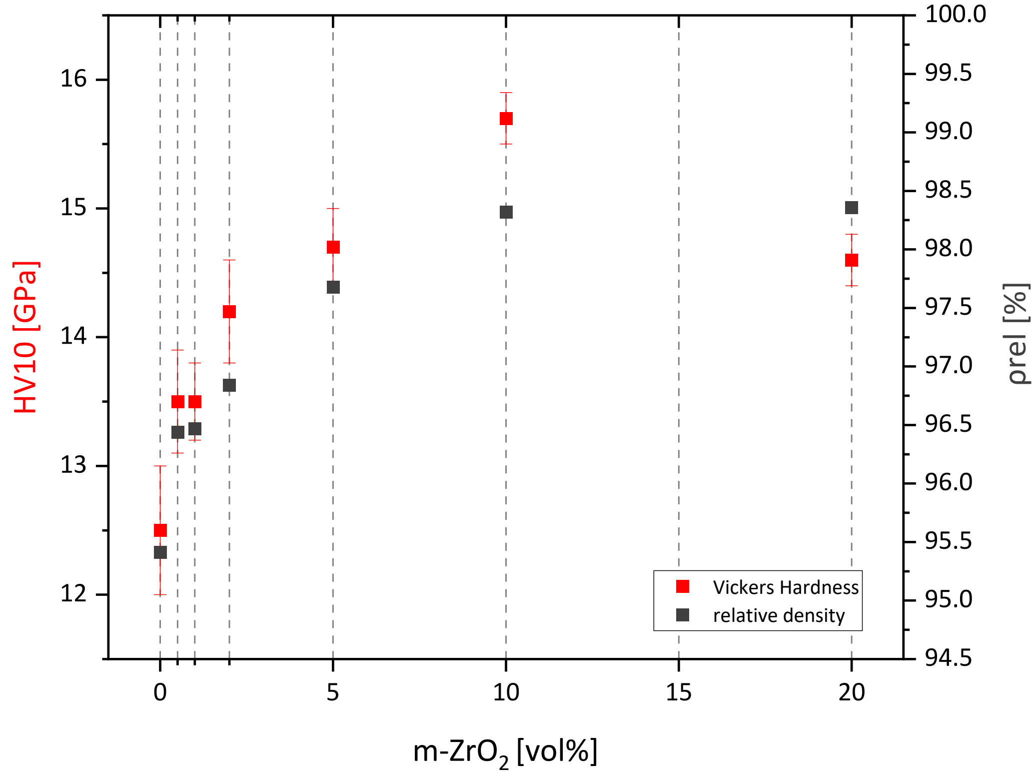

Fig. 26: Comparison of HV10 vs. the relative density for TA with different volume fractions of m-ZrO_2

Fig. 27 a) – f) shows the Vickers imprints for each composition of all materials of study after loading with 10kg. It can be observed, that TA with 10 and 20 vol% zirconia (Fig. 27 e) & f)) have well defined imprints and behave like brittle (equiaxed) materials, i.e. the cracks are emanating from the corners. With decreasing content of the second phase, resulting in an increasing volume fraction of orientated grains, the cracks are rather initiating and propagating along the edges than from the corner of the indent. This might be attributed, as already mentioned for the monolithic TA, to the anisotropy of the textured grains and occurring sliding effects.

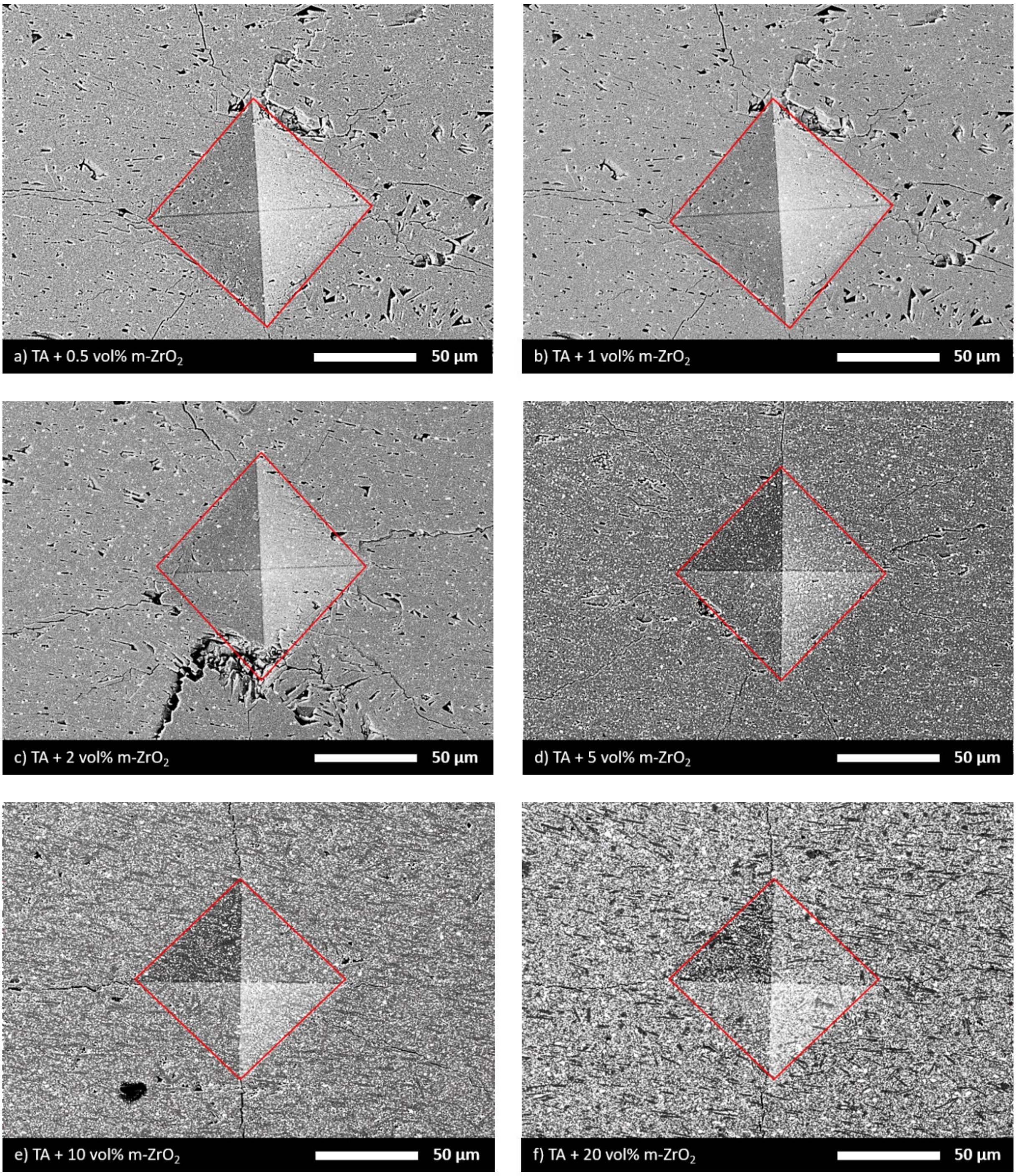

Fig. 27: *SEM micrographs showing the Vickers indentations for TA + increasing volume fraction of zirconia (a) 0.5 vol% m-ZrO$_2$ – f) 20 vol% m-ZrO$_2$)*

4.2.3.2 Fracture Toughness

The fracture toughness for TA with contents of m-ZrO_2 was evaluated parallel ($K_{IC\,//}$) to the (0001) plane of the elongated grains (see Fig. 11). In Table 9 the determined K_{IC} values for the materials of study are listed. Based on the results, it can be stated that the monolithic TA has the highest fracture toughness (≈ 5.4 MPa $m^{1/2}$). Samples with a volume fraction of the second phase ≤ 2.0 vol%, exhibit similar K_{IC} values of approximately 5.1 MPa $m^{1/2}$, considering the standard deviation. The lower measured fracture toughness for these samples compared to monolithic TA might be related to the lower determined aspect ratio (less elongated grains), resulting in the reduction of occurring toughening mechanisms as crack deflection or bifurcation. However, for the samples with m-ZrO_2 ≤ 2.0 vol% microstructural characterization showed that textured microstructure is dominant (LF ≥ 0.2) beneficially affecting the fracture toughness. Though, for samples with volume fractions of m-ZrO_2 ≥ 5 vol%, the fraction of textured grains decreases, resulting in a decrease in fraction toughness, K_{IC} > 4.5 MPa $m^{1/2}$. Nevertheless, the fracture toughness is still higher than the value for monolithic equiaxed alumina, as found in literature (K_{IC} = 3-4 MPa $m^{1/2}$ [29]). Here, it can be assumed that the higher K_{IC} value compared to EA is caused by the second phase, since the K_{IC} values found in literature for zirconia is 5-10 MPa $m^{1/2}$[29]. Furthermore, it can be noted that some samples have a higher standard deviation in comparison to others. On the one hand this might be attributed to the variation in the bulk material caused by fabrication and on the other hand by the sample preparation e.g. different notch – length or – root radius (see appendix).

As already mentioned in chapter 1.2 aims and objectives, one hypothesis was that due to mismatching coefficients of thermal expansion of TA and m-ZrO_2 and the volume increase of m-ZrO_2 during cooling after sintering, induces intrinsic residual compressive stresses. This could lead to an improvement of the resistance against crack propagation of TA. According to fracture toughness, samples with additional m-ZrO_2 did not exhibit higher values in comparison to monolithic TA.

Table 9: *Fracture toughness for TA + 0 – 20 vol% m-ZrO$_2$*

materials	**K_{IC}** [MPa m$^{1/2}$]
TA	5.40 ± 0.21
TA + 0.5 vol% m-ZrO$_2$	4.85 ± 0.30
TA + 1.0 vol% m-ZrO$_2$	5.14 ± 0.08
TA + 2.0 vol% m-ZrO$_2$	5.22 ± 0.42
TA + 5.0 vol% m-ZrO$_2$	4.55 ± 0.22
TA + 10.0 vol% m-ZrO$_2$	4.40 ± 0.09
TA + 20.0 vol% m-ZrO$_2$	4.45 ± 0.04

The optical micrographs in Fig. 28 a.1) – g.1) show the monolithic TA and TA + m-ZrO$_2$ samples of each composition after K_{IC} – testing. The images provide an overview about the fracture behavior of the different composites. Considering TA (see Fig. 28 a.1)) intense crack deflection mechanisms occur. The crack path appears to be highly rough and gradually. With increasing volume fraction of m-ZrO$_2$, this effect is reduced. Until a volume fraction of > 2 vol% second phase the fracture toughness is beneficially influenced by texture. For the composites with ≥ 10 vol% monoclinic zirconia, the crack propagates nearly straight through the bulk material and exhibits a fracture behavior similar to brittle materials.

For detailed understanding of the fractural behavior of textured alumina – zirconia ceramics, SEM micrographs were taken from the fracture path after SEVNB – testing. Fig. 28 a.2) – g.2) displays the fracture path of the monolithic textured alumina, where the crack propagates intergranular along the grain boundaries and is deflected due to the morphology and crystallographic orientation of the textured grains. The same behavior can be observed for the composite material with 0.5 vol% of second phase. From a content of 1 vol% m-ZrO$_2$ it is observed that the crack starts propagating transgranular (see Fig. 28 c.2) – g.2)).

Based on the images following statements can be made: the second phase (i) distributed within grains might weaken the individual grains or (ii) distributed along the grain boundaries might reinforce them. According to (i) it is hypnotized that zirconia placed inside the textured grains of alumina provoke tensile residual stresses due to different coefficients of thermal expansions resulting in a grain weakening. Considering (ii), the second phase placed on the grain boundaries might form strong interfaces based on interaction of tensile and compressive stresses, thus anchoring the grains. For a better understanding of this phenomenon, finite element methods (FEM) could be used. However, this is beyond the scope of this thesis.

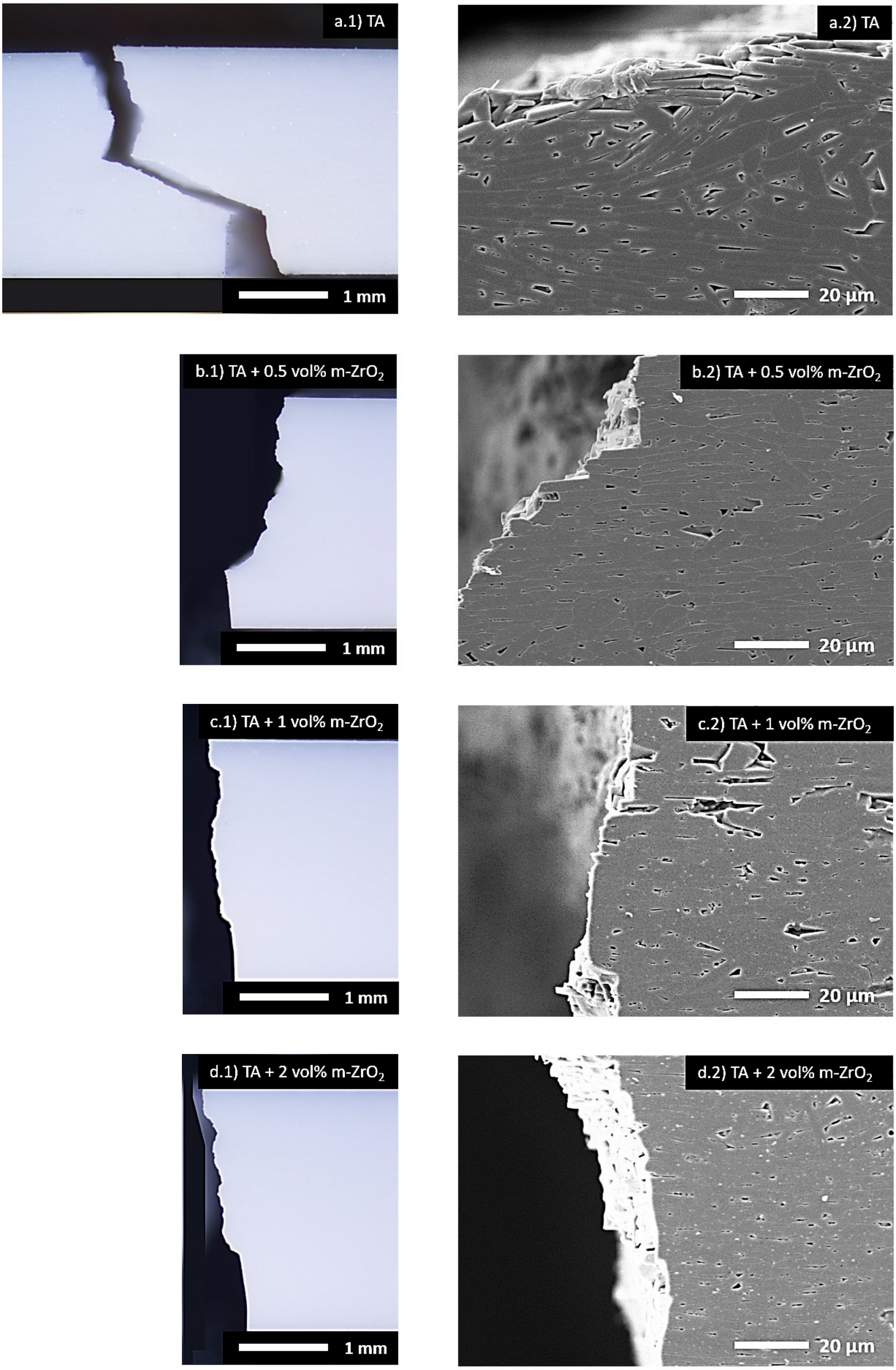
a.1) TA
1 mm
a.2) TA
20 µm
b.1) TA + 0.5 vol% m-ZrO$_2$
1 mm
b.2) TA + 0.5 vol% m-ZrO$_2$
20 µm
c.1) TA + 1 vol% m-ZrO$_2$
1 mm
c.2) TA + 1 vol% m-ZrO$_2$
20 µm
d.1) TA + 2 vol% m-ZrO$_2$
1 mm
d.2) TA + 2 vol% m-ZrO$_2$
20 µm

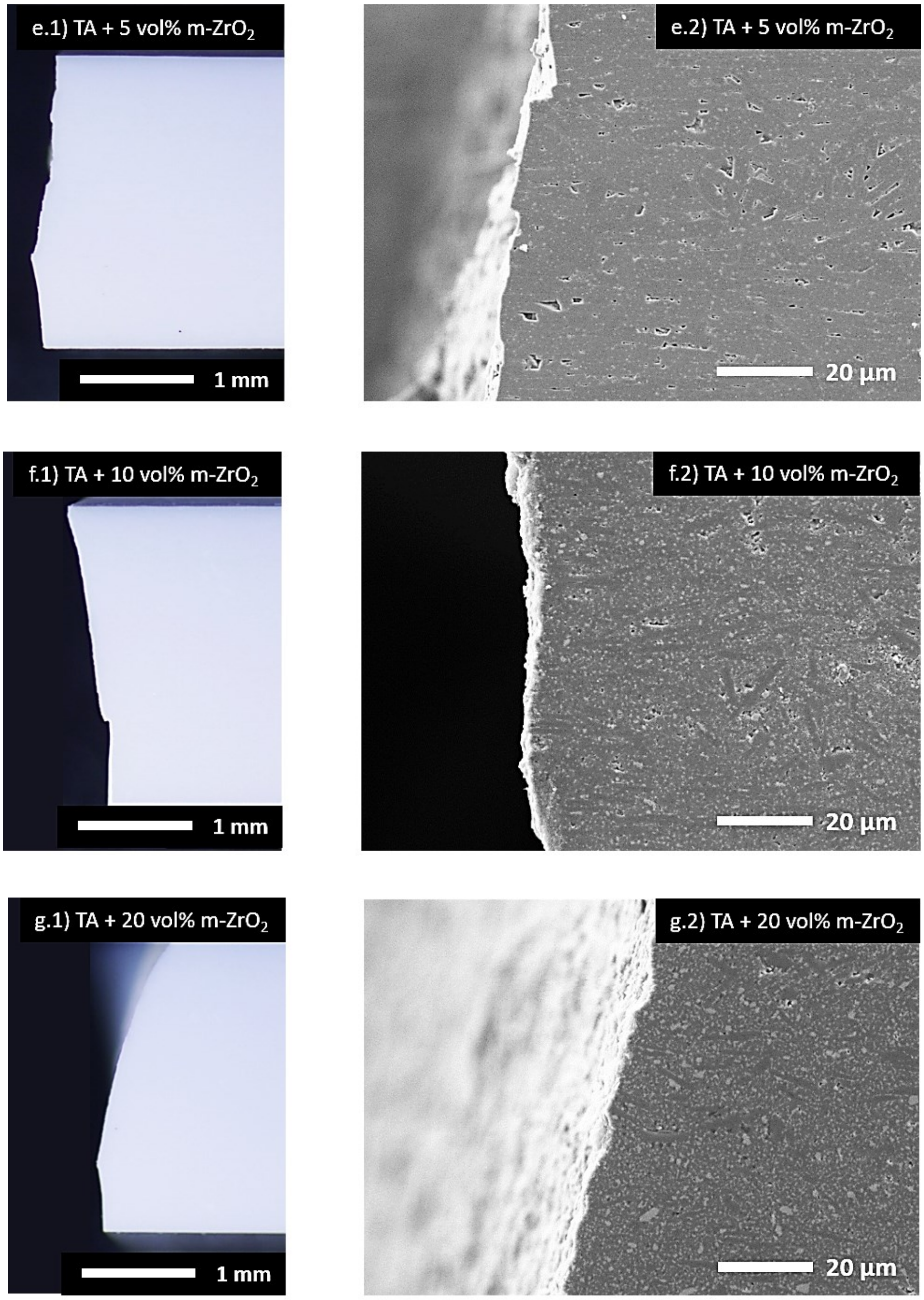

Fig. 28: *a.1 – g.1) Optical micrographs (notch placed on the bottom) and a.2 – g.2) SEM micrographs) observing the crack path after the K_{IC} – measurement of TA + increasing volume fraction of zirconia (a) 0 vol% m-ZrO_2 – g) 20 vol% m-ZrO_2)*

Relation btw. hardness and fracture toughness

An aim of this thesis was to improve and control the hardness of TA by adding monoclinic zirconia as second phase, without losing the beneficial effect of the textured microstructure on toughness. Therefore, the evaluated fracture toughness vs. the Vickers hardness are plotted in Fig. 29. It can be demonstrated that HV10 could be increased from ≈ 12 GPa to ≈ 14 GPa with a volume fraction of 2 vol% m-ZrO_2 without a significant decrease of fracture toughness (TA ≈ 5.4 MPa $m^{1/2}$, TA + 2 vol% m-ZrO_2 ≈ 5.1 MPa $m^{1/2}$). Although the HV10 increases from a content of 5 vol% m-ZrO_2 the fracture toughness strongly decreases due to the reduction of texture. To conclude, it can be approved that the addition of monoclinic zirconia in TA provides the possibility to adjust the hardness without changing the toughness drastically until a content of 2 vol%. However, the solution is as usual a compromise between both.

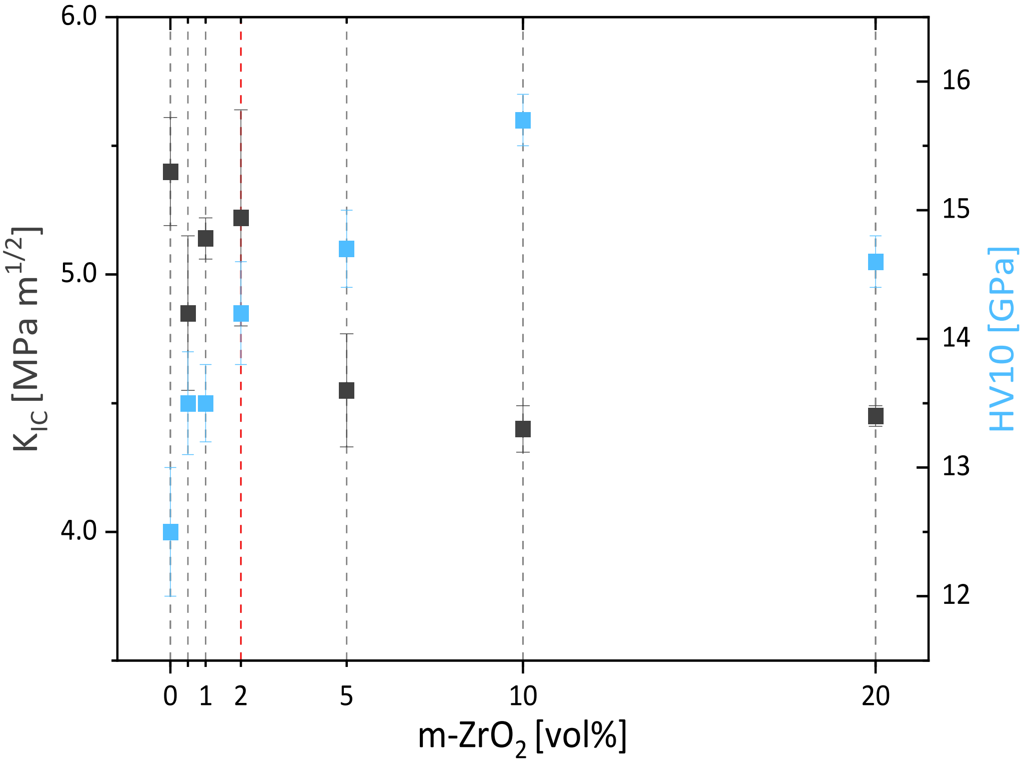

Fig. 29: *Comparison of fracture toughness vs. Vickers hardness*

5. Conclusion

In this thesis, the effect and feasibility of adding a second phase of zirconia to a textured alumina microstructure was explored. The work can be divided into two main tasks: (i) the processing of textured alumina – zirconia ceramics by utilizing the tape casting process for template alignment and the method of TGG for microstructural development; (ii) characterization of the fabricated samples according to their microstructure, their physical as well as mechanical properties.

According to (i) slurries with a viscosity of ≈ 350 mPas were prepared with a non – aqueous system for the tape casting process. The microstructural analysis showed alternating layers of well and irregular oriented grains, which may be related to inconsistent solvent evaporation during the tape casting process. Fractography of the monolithic textured alumina displayed a very homogenous distribution of defects and/or pores, assessing the quality of the processing route to be of high standards. Measured relative densities of higher than 95% for textured microstructures were obtained.

Considering (ii), microstructure was characterized using SEM images and X-Ray diffraction. The quality of texture was determined by comparing XRD patterns, determining the Lotgering Factor (LF). The evaluated LF of e.g. monolithic TA was 0.42, which is comparably low to the desired value of > 0.90. This might be attributed to inhomogeneities found in the microstructure at the surface of the sample. Additionally, for more detailed information about the quality of texture, the Rocking curve was measured and the fitting parameters of the March – Dollase equation determined. According to the XRD measurements, the statements from the analysis of the micrographs were validated that until ≈ 2 vol% of added second phase texture can be observed. An increase of volume fracture of zirconia, results in a typically two – phase, randomly orientated, fine grained microstructure.

Since the characteristics of a ceramic microstructure are mainly responsible for the materials properties, a significant influence on the fracture behavior and damage tolerance was expected due to the addition of the second phase in TA. The hardness was measured after Vickers and the fracture toughness by the Single Edge V – Notched Beam method (SEVNB). With increasing the volume fraction of the second phase, a significant increase of hardness was observed. Monolithic TA occurred to be the softest material with HV10 = 12.5 ± 0.5 GPa and for the sample with 10 vol% of added second phase the highest value was evaluated with HV10 = 15.7 ± 0.2. In comparison EA has a HV10 of ≈ 19 GPa [1]. The highest fracture toughness was determined for monolithic TA with K_{IC} = 5.40 ± 0.21 MPa $m^{1/2}$, even higher than reported for a single crystal alumina ($K_{IC\ (0001)}$ = 4.54 ± 0.21 MPa $m^{1/2}$ [55]), which may be attributed the morphology of the textured microstructure and the resulting energy dissipation caused by crack deflection. With increasing the content of the second phase, the fracture behavior was influenced by the texture until ≈ 2 vol% of added second phase. Increasing the volume fraction of zirconia results in a drop of the K_{IC} value from ≈ 5 MPa $m^{1/2}$ to ≈ 4 MPa $m^{1/2}$, but still higher in comparison to EA alumina ((K_{IC} ≈ 3.5 MPa $m^{1/2}$ [29]).

It can be concluded that the concept of bio – inspired materials has proven to be an effective way to tailor mechanical properties in materials. This work provides further understanding about the influence of the introduction of a second phase onto texture development and material properties in alumina containing ceramics. The addition of a second phase opens the possibility to adjust textured materials' properties, as e.g. hardness, regarding the requirements of application.

6. Future Work

In chapter 4. Results and Discussion it is shown that the hardness of the material strongly depends on the relative density. Therefore, in future work focus will be laid on sintering and processing control porosity but also size and aspect ratio of the grains in TA and investigate its effect on materials properties.

Furthermore, as mentioned in the introduction, ceramics suffer from sub – critical crack growth (SCCG) influenced by humidity and temperature and are very sensitive to rapid cooling. Future work is needed to understand the behavior of textured materials in more detail. This could be achieved by testing at different humidity, temperatures and different constant loads as well as testing under thermal shock conditions.

Additionally, future work should be investigated of the effect by adding other second phases such as tetragonal zirconia (t-ZrO_2) or MAX – Phase (M … transition metal, A … A – group element, X … Carbon/Nitrogen) on mechanical properties and microstructural characteristics of TA. The idea of t-ZrO_2 doped alumina is the benefit of stress – induced phase transformation from tetragonal to monoclinic as known for the ZTA. The idea of the MAX – Phase is the imitation from nature to create a brick and mortar structure by modifying the grain boundaries with a MAX – Phase i.e. “ductile” interface between the textured grains and using the combination of mechanical properties of metals and ceramics; ductility and strength.

All these mentioned approaches for future works are based on tailoring the microstructure. Subsequently, the investigation of processing multi – materials in 2D and or complex 3D architectures with such tailored microstructure materials, would be highly interested. The work should be aiming to using layers with different properties to control the crack propagation (crack deflection in weak interlayers, crack arrest in strong interlayers) or tailoring the magnitude and location of residual stresses in complex 3D structures.

7. References

[1] R. Telle, H. Salmang, H. Scholze (Eds.), Keramik: Mit 132 Tabellen, 7th ed., Springer, Berlin, 2007.

[2] C.B. Carter, M.G. Norton, Ceramic Materials, Springer New York, New York, NY, 2013.

[3] J.J. Gilvarry, B.H. Bergstrom, Fracture of Brittle Solids. II. Distribution Function for Fragment Size in Single Fracture (Experimental), Journal of Applied Physics 32 (1961) 400–410. https://doi.org/10.1063/1.1736017.

[4] S. M. Wiederhorn, Subcritical Crack Growth in Ceramics, Plenum Press, New York, 1974.

[5] R.O. Ritchie, The conflicts between strength and toughness, Nat. Mater. 10 (2011) 817–822. https://doi.org/10.1038/nmat3115.

[6] F.F. Lange, Powder Processing Science and Technology for Increased Reliability, J. Am. Ceram. Soc. 1989 3–15.

[7] M.E. Nordberg, E.L. Mochel, H.M. Garfinkel, J.S. Olcott, Strengthening by ion exchange, J. Am. Ceram. Soc. (1964) 215–219.

[8] Corning Gorilla Glass, Gorilla Glass | Damage and Scratch Resistant Device Glass Protection. https://www.corning.com/gorillaglass/worldwide/en.html (accessed November 2021).

[9] David J. Green, An Introduction to the Mechanical Properties of Ceramics, Cambridge University Press, 1998.

[10] Stefan Fünfschilling, Mikrostrukturelle Einflüsse auf das R-Kurvenverhalten bei Siliciumnitridkeramik, Institut für Keramik und Maschinenbau (2009) 19–21.

[11] E. Munch, M.E. Launey, D.H. Alsem, E. Saiz, A.P. Tomsia, R.O. Ritchie, Tough, Bio-Inspired Hybrid Materials, Science (2008) 1511–1516. https://doi.org/10.1126/science.1160165.

[12] F. Bouville, Strong and tough nacre-like aluminas: Process–structure–performance relationships and position within the nacre-inspired composite landscape, J. Mater. Res. 35 (2020) 1076–1094. https://doi.org/10.1557/jmr.2019.418.

[13] M. Suzuki, H. Nagasawa, Mollusk shell structures and their formation mechanism, Can. J. Zool. 91 (2013) 349–366. https://doi.org/10.1139/cjz-2012-0333.

[14] J. Wu, H. Yuan, L. Li, K. Fan, S. Qian, B. Li, Viscoelastic shear lag model to predict the micromechanical behavior of tendon under dynamic tensile loading, J. Theor. Biol. 437 (2018) 202–213. https://doi.org/10.1016/j.jtbi.2017.10.018.

[15] G.L. Messing, S. Poterala, Y. Chang, T. Frueh, E.R. Kupp, B.H. Watson, R.L. Walton, M.J. Brova, A.-K. Hofer, R. Bermejo, R.J. Meyer, Texture-engineered ceramics—Property enhancements through crystallographic tailoring, J. Mater. Res. 32 (2017) 3219–3241. https://doi.org/10.1557/jmr.2017.207.

[16] R. Bermejo, “Toward seashells under stress”: Bioinspired concepts to design tough layered ceramic composites, Journal of the European Ceramic Society 37 (2017) 3823–3839. https://doi.org/10.1016/j.jeurceramsoc.2017.04.041.

[17] X. Zhang, W. Wu, J. Wang, Dynamic analysis of preferential orientation of aragonite crystals in nacre from mollusk shell, Chin. Sci. Bull. 52 (2007) 3452–3456. https://doi.org/10.1007/s11434-007-0483-7.

[18] A. Goyal, R. Feenstra, F.A. List, M. Paranthaman, D.F. Lee, Using RABiTS to fabricate high-temperature superconducting wire, JOM 51 (1999).

[19] S. Jin, R.C. Sherwood, R.B. van Dover, T.H. Tiefel, and, High TC superconductors-composite wire fabrication, Appl. Phys. Lett. 51 (1987).

[20] Y. Sakka and T.S. Suzuki, Textured development of feeble magnetic ceramics by colloidal processing under high magnetic field, J. Ceram. Soc. Jpn. 113 (2005).

[21] T. Tani, n. Appl. Phys. Lett. 51, 203 (1987). 13. T. Tani: Texture engineering of electronic ceramics by the reactive-templated grain growth method, J. Ceram. Soc. Jpn. 114 (2006).

[22] H. Yilmaz, G.L. Messing, and S. Trolier-McKinstry, (Reactive) templated grain growth of textured sodium bismuth titanate (Na1/2Bi1/2TiO3–BaTiO3) ceramics–I, Processing. J. Electroceram 11 (2003).

[23] J.J. Went, G.W. Rathenau, E.W. Gorter, and G.W. van Oosterhout, Hexagonal iron-oxide compounds as permanent-magnet materials, Physical Review 86 (1952) 424–425.

[24] S. Deville, Ice-templating, freeze casting: Beyond materials processing, J. Mater. Res. 28 (2013) 2202–2219. https://doi.org/10.1557/jmr.2013.105.

[25] H. Le Ferrand, F. Bouville, T.P. Niebel, and A.R. Studart, Magnetically assisted slip casting of bioinspired heterogeneous composites, Nat. Mater 14 (2015) 1172–1179.

[26] K. Evers, S. Falco, N. Grobert, and R. Todd, Nacre-like alumina with unique high strain rate capabilities, J Am Ceram Soc 40 (2019) 417–426.

[27] G.M. R.J. Pavlacka, Processing and mechanical response of highly textured Al2O3, Journal of the European Ceramic Society 30 (2010) 2917–2925.

[28] A.-K. Hofer, R. Walton, O. Ševeček, G.L. Messing, R. Bermejo, Design of damage tolerant and crack-free layered ceramics with textured microstructure, Journal of the European Ceramic Society 40 (2020) 427–435. https://doi.org/10.1016/j.jeurceramsoc.2019.09.004.

[29] M.F. Ashby, Materials Selection in Mechanical Design (1993).

[30] Richard E. Mistler and Eric R. Twiname, TAPE CASTING: THEORY AND PRACTICE.

[31] R.L. Walton, M.D. Vaudin, A.-K. Hofer, E. Kupp, R.J. Meyer, G.L. Messing, Tailoring Particle Alignment and Grain Orientation during Tape Casting and Templated Grain Growth, J Am Ceram Soc (2018). https://doi.org/10.1111/jace.16144.

[32] Hyun Jun Kim, Matthew John M. Krane, Kevin P. Trumble, and Keith J. Bowman, Analytical Fluid Flow Models for Tape Casting, J. American Ceramic Society (Journal of the American Ceramic Society) (2006) 2769–2775. https://doi.org/10.1111/j.1551-2916.2006.01163.x.

[33] P. W. Voorhees, The Theory of Ostwald Ripening, Journal of Statistical Physics 38 (1985) 231–252.

[34] M.M. Seabaugh, G.L. Messing, M.D. Vaudin, Texture Development and Microstructure Evolution in Liquid-Phase-Sintered α-Alumina Ceramics Prepared by Templated Grain Growth, Journal of the American Ceramic Society 83 (2000) 3109–3116. https://doi.org/10.1111/j.1151-2916.2000.tb01690.x.

[35] M.N. Rahaman, Sintering of Ceramics, Taylor and Francis, Hoboken, 2007.

[36] R.M. German, P. Suri, S.J. Park, Review: liquid phase sintering, J Mater Sci 44 (2009) 1–39. https://doi.org/10.1007/s10853-008-3008-0.

[37] J. Wang and R. Stevens, Zirconia-toughened alumina (ZTA) ceramics, J Mater Sci 24 (1989) 3421–3440.

[38] Ronald G. Munro, Evaluated Material Properties for a Sintered alpha-Alumina, J. Am. Ceram. Soc. 80 (1997) 1919–1928.

[39] W. E. Lee and W. M. Rainforth, Ceramic Microstructures, Chapman & Hall, London, 1994.

[40] P. Auerkari, Mechanical and physical properties of engineering alumina ceramics, Technical Research Centre of Finland (1996).

[41] J. Eichler, U. Eisele, J. Rödel, Mechanical Properties of Monoclinic Zirconia, Journal of the American Ceramic Society 87 (2004) 1401–1403. https://doi.org/10.1111/j.1151-2916.2004.tb07748.x.

[42] ÖNORM, Hochleistungskeramik - Prüfverfahren zur Bestimmung der Bruchzähigkeit monolothischer Keramik: Verfahren für Biegeproben mit V-Kerbe (SEVNB-Verfahren), 2016.

[43] T. Nishida, Y. Hanaki, G. Pezzotti, Effect of Notch-Root Radius on the Fracture Toughness of a Fine-Grained Alumina, J American Ceramic Society 77 (1994) 606–608. https://doi.org/10.1111/j.1151-2916.1994.tb07038.x.

[44] ÖNORM, Hochleistungskeramik - Mechanische Eigenschaften monolithische Keramik bei Raumtemperatur: Teil 1: Bestimmung der Biegefestigkeit, 2008.

[45] F.K. Lotgering, Topotactical reactions with ferrimagnetic oxides having hexagonal crystal structures—I, J. Inorg. Nucl. Chem 9 (1959) 113–123.

[46] M.D. Vaudin, M.W. Rupich, M. Jowett, G.N. Riley, J.F. Bingert, A method for crystallographic texture investigations using standard x-ray equipment, J. Mater. Res. 13 (1998) 2910–2919. https://doi.org/10.1557/JMR.1998.0398.

[47] ÖNORM, Hochleistungskeramik - Monolithische Keramik-Allgemeine und strukturelle Eigenschaften: Teil 2: Bestimmung von Dichte und Porosität, 1994.

[48] ÖNORM, Hochleistungskeramik - Mechanische Eigenschaften monolithische Keramik bei Raumtemperatur: Teil 2: Bestimmung des Elastizitätsmoduls, Schubmuduls und der Poissonzahl.

[49] ÖNORM, Hochleistungskeramik -Mechanische Eigenschaften monolithische Keramik bei Raumtemperatur: Teil 4: Härteprüfung nach Vickers,Knoop und Rockwell, 2005.

[50] DIN, Hochleistungskeramik - Prüfverfahren zur Bestimmung der Bruchzähigkeit monolithischer Keramik bei Raumtemperatur an einseitig gekerbten Biegeproben (SEPB-Verfahren), 2005.

[51] M. Zhang, Y. Chang, R. Bermejo, G. Jiang, Y. Sun, J. Wu, B. Yang, W. Cao, Improved fracture behavior and mechanical properties of alumina textured ceramics, Mater. Lett. 221 (2018) 252–255.

[52] J.A. Choren, S.M. Heinrich, M.B. Silver-Thorn, Young’s modulus and volume porosity relationships for additive manufacturing applications, J Mater Sci 48 (2013) 5103–5112. https://doi.org/10.1007/s10853-013-7237-5.

[53] Mc Colm, Ceramic Hardness, Plenum Press, New York (1990).

[54] T. Carisey, I. Levin, and D.G. Brandon, Microstructure and mechanical properties of textured Al2O3, J. Eur. Ceram. Soc. 283 (1995).

[55] M. Iwasa, R. C. Brandt, Fracture Toughness of Single-Crystal Alumina, Advances in ceramics 1984 767–774.

[56] W. Weibull (Ed.), A Statistical Theory of the Strength of Materials, Generalstabens litografiska anstalts forlag, Stockholm, 1939.

[57] W. Weibull, A statistical distribution function of wide applicability, J. Appl. Mech. (1951) 293–297.

[58] Munz, D. and Fett, T., Ceramics. Mechanical Properties, Failure Behaviour, Materials Selection, Materials science 36 (2001).

[59] Yu.V. Milman a, S.I. Chugunova, I.V. Goncharova, W. Gooch, Temperature dependence of hardness in silicon±carbide ceramics with dierent porosity, International Journal of refractory metals and hard materials 17 (1999) 361–368.

8. List of Tables

9. List of Figures

10. Appendix

10.1. Experimental Data

Table 10: Measured strength values of TA

ID	F [N]	σ_f [MPa]
S21007_4	205.12	261.17
S21006_4	220.55	269.93
S21006_6	221.68	271.63
S21004_6	270.45	274.62
S21006_1	229.16	278.36
S21005_3	227.44	278.52
S21004_1	268.27	280.97
S21007_3	227.26	282.28
S21004_4	278.35	284.47
S21006_3	230.36	285.76
S21004_7	270.97	286.22
S21005_1	228.88	286.98
S21005_5	238.41	287.94
S21005_7	243.82	289.24
S21006_7	233.79	289.64
S21006_5	226.95	290.18
S21005_2	234.47	291.93
S21006_2	234.41	292.21
S21005_6	238.17	292.48
S21005_4	239.15	295.30
S21004_5	286.11	297.80
S21007_1	238.43	299.90
S21007_2	239.67	303.68
S21003_6	310.33	326.89
S21004_2	318.87	329.13
S21003_4	314.19	333.45
S21003_3	311.48	335.35
S21004_3	325.30	335.92
S21003_2	316.56	344.53

Table 11: *Evaluated diagonals of Vickers indentations for TA*

ID S21003-4 #	**d_1 [µm]**	**d_2 [µm]**	**d [mm]**	**d^2 [mm^2]**	**HV [-]**	**HV [GPa]**	**H [GPa]**
1	115.7	120.6	0.118150	0.013959	1326.8	13.02	14.04
2	115.4	124.4	0.119900	0.014376	1288.4	12.64	13.63
3	118.7	124.1	0.121400	0.014738	1256.8	12.33	13.30
4	119.5	127.2	0.123350	0.015215	1217.3	11.94	12.88
5	122.5	125.8	0.124150	0.015413	1201.7	11.79	12.72
6	118.5	124.4	0.121450	0.014750	1255.7	12.32	13.29
7	114.5	119.7	0.117100	0.013712	1350.7	13.25	14.29
8	115.2	124.0	0.119600	0.014304	1294.9	12.70	13.70
9	119.4	125.8	0.122600	0.015031	1232.3	12.09	13.04
10	120.1	129.8	0.124950	0.015613	1186.4	11.64	12.55
				average	**1261**	**12.4**	**13.3**
				st.deviation	**54**	**0.5**	**0.6**

Table 12: *Evaluated diagonals of Vickers indentations for TA*

ID S21004-5 #	**d_1 [µm]**	**d_2 [µm]**	**d [mm]**	**d^2 [mm^2]**	**HV [-]**	**HV [GPa]**	**H [GPa]**
1	116.3	123.1	0.119700	0.014328	1292.7	12.68	13.68
2	113.7	119.8	0.116750	0.013631	1358.9	13.33	14.38
3	121.9	126.0	0.123950	0.015364	1205.6	11.83	12.76
4	117.4	121.5	0.119450	0.014268	1298.1	12.73	13.74
5	116.9	119.8	0.118350	0.014007	1322.4	12.97	13.99
6	119.8	122.3	0.121050	0.014653	1264.0	12.40	13.38
7	119.6	118.8	0.119200	0.014209	1303.6	12.79	13.79
8	118.4	123.1	0.120750	0.014581	1270.3	12.46	13.44
9	117.9	118.7	0.118300	0.013995	1323.5	12.98	14.01
10	116.3	120.6	0.118450	0.014030	1320.1	12.95	13.97
				average	**1296**	**12.7**	**13.7**
				st.deviation	**42**	**0.4**	**0.4**

Table 13: *Evaluated diagonals of Vickers indentations for TA + 0.5 vol% ZrO$_2$*

ID S21019-2 #	d_1 [µm]	d_2 [µm]	d [mm]	d^2 [mm^2]	HV [-]	HV [GPa]	H [GPa]
1	116.6	119.6	0.118100	0.013948	1328.0	13.03	14.05
2	117.6	118.6	0.118100	0.013948	1328.0	13.03	14.05
3	111.9	119.4	0.115650	0.013375	1384.8	13.58	14.65
4	121.9	116.6	0.119250	0.014221	1302.5	12.78	13.78
5	112.0	119.2	0.115600	0.013363	1386.0	13.60	14.67
6	118.0	112.9	0.115450	0.013329	1389.6	13.63	14.71
7	118.8	110.5	0.114650	0.013145	1409.1	13.82	14.91
8	113.7	117.2	0.115450	0.013329	1389.6	13.63	14.71
9	112.1	120.5	0.116300	0.013526	1369.4	13.43	14.49
10	110.1	117.4	0.113750	0.012939	1431.5	14.04	15.15
				average	**1372**	**13.5**	**14.5**
				st.deviation	**40**	**0.4**	**0.4**

Table 14: *Evaluated diagonals of Vickers indentations for TA + 1.0 vol% ZrO$_2$*

ID S21018-2 #	d_1 [µm]	d_2 [µm]	d [mm]	d^2 [mm^2]	HV [-]	HV [GPa]	H [GPa]
1	120.0	114.7	0.117350	0.013771	1345.0	13.19	14.23
2	116.0	117.7	0.116850	0.013654	1356.5	13.31	14.35
3	118.1	115.4	0.116750	0.013631	1358.9	13.33	14.38
4	112.7	117.3	0.115000	0.013225	1400.5	13.74	14.82
5	111.1	117.0	0.114050	0.013007	1424.0	13.97	15.07
6	114.5	120.4	0.117450	0.013795	1342.7	13.17	14.21
7	117.3	116.2	0.116750	0.013631	1358.9	13.33	14.38
8	114.4	119.7	0.117050	0.013701	1351.9	13.26	14.31
9	111.9	118.6	0.115250	0.013283	1394.5	13.68	14.76
10	116.6	113.2	0.114900	0.013202	1403.0	13.76	14.85
				average	**1374**	**13.5**	**14.5**
				st.deviation	**29**	**0.3**	**0.3**

Table 15*: Evaluated diagonals of Vickers indentations for TA + 2.0 vol% ZrO_2*

ID S21016-2 #	d_1 [µm]	d_2 [µm]	d [mm]	d^2 [mm^2]	HV [-]	HV [GPa]	H [GPa]
1	114.0	115.2	0.114600	0.013133	1410.3	13.83	14.92
2	108.3	119.0	0.113650	0.012916	1434.0	14.07	15.17
3	109.8	116.3	0.113050	0.012780	1449.3	14.22	15.34
4	109.1	118.6	0.113850	0.012962	1429.0	14.02	15.12
5	115.2	108.6	0.111900	0.012522	1479.2	14.51	15.65
6	109.2	113.1	0.111150	0.012354	1499.2	14.71	15.86
7	109.9	118.3	0.114100	0.013019	1422.7	13.96	15.06
8	107.8	114.1	0.110950	0.012310	1504.6	14.76	15.92
9	110.1	114.3	0.112200	0.012589	1471.3	14.43	15.57
10	118.4	114.0	0.116200	0.013502	1371.8	13.46	14.52
				average	**1447**	**14.2**	**15.3**
				st.deviation	**42**	**0.4**	**0.4**

Table 16: *Evaluated diagonals of Vickers indentations for TA + 5.0 vol% ZrO_2*

ID S21013-2 #	d_1 [µm]	d_2 [µm]	d [mm]	d^2 [mm^2]	HV [-]	HV [GPa]	H [GPa]
1	108.8	111.4	0.110100	0.012122	1528.0	14.99	16.17
2	108.8	115.2	0.112000	0.012544	1476.6	14.48	15.63
3	108.0	111.9	0.109950	0.012089	1532.1	15.03	16.21
4	110.5	114.3	0.112400	0.012634	1466.1	14.38	15.51
5	108.8	114.4	0.111600	0.012455	1487.2	14.59	15.74
6	110.5	114.4	0.112450	0.012645	1464.8	14.37	15.50
7	107.7	112.9	0.110300	0.012166	1522.4	14.93	16.11
8	107.6	111.9	0.109750	0.012045	1537.7	15.08	16.27
9	109.6	113.5	0.111550	0.012443	1488.5	14.60	15.75
10	112.7	114.5	0.113600	0.012905	1435.3	14.08	15.19
				average	**1494**	**14.7**	**15.8**
				st.deviation	**35**	**0.3**	**0.4**

Table 17: *Evaluated diagonals of Vickers indentations for TA + 10.0 vol%* ZrO_2

ID S21012-2 #	d_1 [µm]	d_2 [µm]	d [mm]	d^2 [mm^2]	HV [-]	HV [GPa]	H [GPa]
1	107.0	108.6	0.107800	0.011621	1593.9	15.64	16.87
2	108.4	109.4	0.108900	0.011859	1561.8	15.32	16.53
3	105.8	108.8	0.107300	0.011513	1608.7	15.78	17.02
4	106.8	109.0	0.107900	0.011642	1590.9	15.61	16.84
5	106.8	109.4	0.108100	0.011686	1585.0	15.55	16.77
6	105.8	108.7	0.107250	0.011503	1610.2	15.80	17.04
7	106.7	107.8	0.107250	0.011503	1610.2	15.80	17.04
8	106.4	108.3	0.107350	0.011524	1607.3	15.77	17.01
9	106.7	110.2	0.108450	0.011761	1574.8	15.45	16.66
10	104.4	108.3	0.106350	0.011310	1637.6	16.06	17.33
				average	**1598**	**15.7**	**16.9**
				st.deviation	**21**	**0.2**	**0.2**

Table 18: *Evaluated diagonals of Vickers indentations for TA + 20.0 vol%* ZrO_2

ID S21010-2 #	d_1 [µm]	d_2 [µm]	d [mm]	d^2 [mm^2]	HV [-]	HV [GPa]	H [GPa]
1	112.4	110.0	0.111200	0.012365	1497.9	14.69	15.85
2	112.8	112.1	0.112450	0.012645	1464.8	14.37	15.50
3	111.4	110.7	0.111050	0.012332	1501.9	14.73	15.89
4	112.1	112.8	0.112450	0.012645	1464.8	14.37	15.50
5	110.1	112.1	0.111100	0.012343	1500.6	14.72	15.88
6	111.4	113.1	0.112250	0.012600	1470.0	14.42	15.56
7	111.2	110.8	0.111000	0.012321	1503.3	14.75	15.91
8	110.5	112.9	0.111700	0.012477	1484.5	14.56	15.71
9	110.3	112.0	0.111150	0.012354	1499.2	14.71	15.86
10	110.8	111.5	0.111150	0.012354	1499.2	14.71	15.86
				average	**1489**	**14.6**	**15.8**
				st.deviation	**16**	**0.2**	**0.2**

Fracture Toughness

Table 19: *TA liegend*

ID	B [mm]	W [mm]	F [N]	α [-]	σ_f [MPa]	ρ [µm]	Y* [-]	K_{IC} [MPa $m^{1/2}$]
S21001_1	3.897	2.581	82.82	0.298	95.7	5.000	1.990	5.28
S21001_2	3.945	2.616	78.72	0.338	87.5	3.000	2.068	5.38
S21001_6	3.971	2.606	83.64	0.323	93.0	3.500	2.037	5.50
S21002_1	3.958	2.630	96.32	0.285	105.5	4.500	1.969	5.69
S21002_6	3.982	2.633	86.97	0.288	94.5	5.000	1.974	5.14

Table 20: *TA stehend*

ID	B [mm]	W [mm]	F [N]	α [-]	σ_f [MPa]	ρ [µm]	Y* [-]	K_{IC} [MPa $m^{1/2}$]
S21001_4	2.604	3.970	97.50	0.234	71.3	4.500	1.906	4.14
S21001_5	2.619	3.983	97.18	0.251	70.2	3.000	1.924	4.27
S21002_3	2.643	3.983	102.12	0.201	73.1	3.000	1.880	3.89
S21002_4	2.621	3.858	96.32	0.218	74.1	2.500	1.892	4.06
S21002_5	2.622	3.992	109.57	0.201	78.7	4.000	1.880	4.19

Table 21: *TA + 0.5 vol% m-ZrO_2*

ID	B [mm]	W [mm]	F [N]	α [-]	σ_f [MPa]	ρ [µm]	Y* [-]	K_{IC} [MPa $m^{1/2}$]
S21019_1	3.729	2.849	97.98	0.217	97.1	1.900	1.891	4.57
S21019_2	3.767	2.750	99.95	0.237	105.2	2.150	1.908	5.12
S21019_3	3.985	2.766	100.36	0.233	98.8	2.500	1.905	4.78
S21019_4	3.969	2.641	96.74	0.253	104.8	1.350	1.926	5.21
S21019_5	3.993	2.845	105.81	0.215	98.2	4.400	1.889	4.59

Table 22: *TA + 1.0 vol% m-ZrO_2*

ID	B [mm]	W [mm]	F [N]	α [-]	σ_f [MPa]	ρ [µm]	Y* [-]	K_{IC} [MPa $m^{1/2}$]
S21018_1	3.736	2.868	108.52	0.235	105.9	3.750	1.907	5.24
S21018_2	3.770	2.900	110.18	0.230	104.2	2.900	1.902	5.12
S21018_3	3.987	2.812	115.36	0.219	109.8	1.700	1.893	5.16
S21018_4	3.947	2.913	115.04	0.226	103.0	4.650	1.898	5.01
S21018_5	3.969	2.866	116.57	0.223	107.3	3.450	1.896	5.14

Table 23: *TA + 2.0 vol% m-ZrO$_2$*

ID	B [mm]	W [mm]	F [N]	α [-]	σ_f [MPa]	ρ [µm]	Y* [-]	K_{IC} [MPa $m^{1/2}$]
S21016_1	3.744	2.795	100.88	0.223	103.4	3.450	1.896	4.90
S21016_2	3.722	2.883	101.25	0.303	98.2	2.350	1.998	5.80
S21016_3	3.962	2.699	98.85	0.223	102.7	2.600	1.896	4.78
S21016_4	3.946	2.913	131.39	0.209	117.7	3.250	1.885	5.48
S21016_5	3.961	2.764	108.12	0.231	107.2	1.250	1.903	5.16

Table 24: *TA + 5.0 vol% m-ZrO$_2$*

ID	B [mm]	W [mm]	F [N]	α [-]	σ_f [MPa]	ρ [µm]	Y* [-]	K_{IC} [MPa $m^{1/2}$]
S21013_1	3.773	2.729	92.80	0.225	99.1	2.150	1.897	4.66
S21013_2	3.761	2.680	71.07	0.281	79.0	3.700	1.963	4.26
S21013_3	3.983	2.765	100.59	0.232	99.1	1.650	1.904	4.78
S21013_4	3.986	2.701	87.72	0.238	90.5	2.900	1.910	4.39
S21013_5	3.880	2.701	84.23	0.268	89.3	2.800	1.944	4.67

Table 25: *TA + 10.0 vol% m-ZrO$_2$*

ID	B [mm]	W [mm]	F [N]	α [-]	σ_f [MPa]	ρ [µm]	Y* [-]	K_{IC} [MPa $m^{1/2}$]
S21012_1	3.659	2.814	82.98	0.259	85.9	2.850	1.933	4.48
S21012_3	3.978	2.781	99.09	0.212	96.6	2.300	1.888	4.43
S21012_4	3.950	2.809	98.55	0.221	94.8	2.200	1.894	4.47
S21012_5	3.911	2.840	100.24	0.205	95.3	1.950	1.882	4.33
S21012_6	3.980	2.743	78.03	0.283	78.2	2.500	1.966	4.28

Table 26: *TA + 20.0 vol% m-ZrO$_2$*

ID	B [mm]	W [mm]	F [N]	α [-]	σ_f [MPa]	ρ [µm]	Y* [-]	K_{IC} [MPa $m^{1/2}$]
S21010_1	3.623	2.761	86.54	0.230	94.0	4.350	1.902	4.50
S21010_2	3.750	2.757	88.33	0.228	92.9	1.750	1.900	4.42
S21010_3	3.921	2.748	87.47	0.250	88.6	1.700	1.922	4.46
S21010_4	3.970	2.766	83.78	0.270	82.7	4.650	1.948	4.41
S21010_7	3.888	2.746	86.66	0.250	88.6	1.200	1.923	4.47

11. References

[1] R. Telle, H. Salmang, H. Scholze (Eds.), Keramik: Mit 132 Tabellen, 7th ed., Springer, Berlin, 2007.

[2] C.B. Carter, M.G. Norton, Ceramic Materials, Springer New York, New York, NY, 2013.

[3] J.J. Gilvarry, B.H. Bergstrom, Fracture of Brittle Solids. II. Distribution Function for Fragment Size in Single Fracture (Experimental), Journal of Applied Physics 32 (1961) 400–410. https://doi.org/10.1063/1.1736017.

[4] S. M. Wiederhorn, Subcritical Crack Growth in Ceramics, Plenum Press, New York, 1974.

[5] R.O. Ritchie, The conflicts between strength and toughness, Nat. Mater. 10 (2011) 817–822. https://doi.org/10.1038/nmat3115.

[6] F.F. Lange, Powder Processing Science and Technology for Increased Reliability, J. Am. Ceram. Soc. 1989 3–15.

[7] M.E. Nordberg, E.L. Mochel, H.M. Garfinkel, J.S. Olcott, Strengthening by ion exchange, J. Am. Ceram. Soc. (1964) 215–219.

[8] Corning Gorilla Glass, Gorilla Glass | Damage and Scratch Resistant Device Glass Protection. https://www.corning.com/gorillaglass/worldwide/en.html (accessed November 2021).

[9] David J. Green, An Introduction to the Mechanical Properties of Ceramics, Cambridge University Press, 1998.

[10] Stefan Fünfschilling, Mikrostrukturelle Einflüsse auf das R-Kurvenverhalten bei Siliciumnitridkeramik, Institut für Keramik und Maschinenbau (2009) 19–21.

[11] E. Munch, M.E. Launey, D.H. Alsem, E. Saiz, A.P. Tomsia, R.O. Ritchie, Tough, Bio-Inspired Hybrid Materials, Science (2008) 1511–1516. https://doi.org/10.1126/science.1160165.

[12] F. Bouville, Strong and tough nacre-like aluminas: Process–structure–performance relationships and position within the nacre-inspired composite landscape, J. Mater. Res. 35 (2020) 1076–1094. https://doi.org/10.1557/jmr.2019.418.

[13] M. Suzuki, H. Nagasawa, Mollusk shell structures and their formation mechanism, Can. J. Zool. 91 (2013) 349–366. https://doi.org/10.1139/cjz-2012-0333.

[14] J. Wu, H. Yuan, L. Li, K. Fan, S. Qian, B. Li, Viscoelastic shear lag model to predict the micromechanical behavior of tendon under dynamic tensile loading, J. Theor. Biol. 437 (2018) 202–213. https://doi.org/10.1016/j.jtbi.2017.10.018.

[15] G.L. Messing, S. Poterala, Y. Chang, T. Frueh, E.R. Kupp, B.H. Watson, R.L. Walton, M.J. Brova, A.-K. Hofer, R. Bermejo, R.J. Meyer, Texture-engineered ceramics—Property enhancements through crystallographic tailoring, J. Mater. Res. 32 (2017) 3219–3241. https://doi.org/10.1557/jmr.2017.207.

[16] R. Bermejo, "Toward seashells under stress": Bioinspired concepts to design tough layered ceramic composites, Journal of the European Ceramic Society 37 (2017) 3823–3839. https://doi.org/10.1016/j.jeurceramsoc.2017.04.041.

[17] X. Zhang, W. Wu, J. Wang, Dynamic analysis of preferential orientation of aragonite crystals in nacre from mollusk shell, Chin. Sci. Bull. 52 (2007) 3452–3456. https://doi.org/10.1007/s11434-007-0483-7.

[18] A. Goyal, R. Feenstra, F.A. List, M. Paranthaman, D.F. Lee, Using RABiTS to fabricate high-temperature superconducting wire, JOM 51 (1999).

[19] S. Jin, R.C. Sherwood, R.B. van Dover, T.H. Tiefel, and, High TC superconductors-composite wire fabrication, Appl. Phys. Lett. 51 (1987).

[20] Y. Sakka and T.S. Suzuki, Textured development of feeble magnetic ceramics by colloidal processing under high magnetic field, J. Ceram. Soc. Jpn. 113 (2005).

[21] T. Tani, n. Appl. Phys. Lett. 51, 203 (1987). 13. T. Tani: Texture engineering of electronic ceramics by the reactive-templated grain growth method, J. Ceram. Soc. Jpn. 114 (2006).

[22] H. Yilmaz, G.L. Messing, and S. Trolier-McKinstry, (Reactive) templated grain growth of textured sodium bismuth titanate (Na1/2Bi1/2TiO3–BaTiO3) ceramics–I, Processing. J. Electroceram 11 (2003).

[23] J.J. Went, G.W. Rathenau, E.W. Gorter, and G.W. van Oosterhout, Hexagonal iron-oxide compounds as permanent-magnet materials, Physical Review 86 (1952) 424–425.

[24] S. Deville, Ice-templating, freeze casting: Beyond materials processing, J. Mater. Res. 28 (2013) 2202–2219. https://doi.org/10.1557/jmr.2013.105.

[25] H. Le Ferrand, F. Bouville, T.P. Niebel, and A.R. Studart, Magnetically assisted slip casting of bioinspired heterogeneous composites, Nat. Mater 14 (2015) 1172–1179.

[26] K. Evers, S. Falco, N. Grobert, and R. Todd, Nacre-like alumina with unique high strain rate capabilities, J Am Ceram Soc 40 (2019) 417–426.

[27] G.M. R.J. Pavlacka, Processing and mechanical response of highly textured Al2O3, Journal of the European Ceramic Society 30 (2010) 2917–2925.

[28] A.-K. Hofer, R. Walton, O. Ševeček, G.L. Messing, R. Bermejo, Design of damage tolerant and crack-free layered ceramics with textured microstructure, Journal of the European Ceramic Society 40 (2020) 427–435. https://doi.org/10.1016/j.jeurceramsoc.2019.09.004.

[29] M.F. Ashby, Materials Selection in Mechanical Design (1993).

[30] Richard E. Mistler and Eric R. Twiname, TAPE CASTING: THEORY AND PRACTICE.

[31] R.L. Walton, M.D. Vaudin, A.-K. Hofer, E. Kupp, R.J. Meyer, G.L. Messing, Tailoring Particle Alignment and Grain Orientation during Tape Casting and Templated Grain Growth, J Am Ceram Soc (2018). https://doi.org/10.1111/jace.16144.

[32] Hyun Jun Kim, Matthew John M. Krane, Kevin P. Trumble, and Keith J. Bowman, Analytical Fluid Flow Models for Tape Casting, J. American Ceramic Society (Journal of the American Ceramic Society) (2006) 2769–2775. https://doi.org/10.1111/j.1551-2916.2006.01163.x.

[33] P. W. Voorhees, The Theory of Ostwald Ripening, Journal of Statistical Physics 38 (1985) 231–252.

[34] M.M. Seabaugh, G.L. Messing, M.D. Vaudin, Texture Development and Microstructure Evolution in Liquid-Phase-Sintered α-Alumina Ceramics Prepared by Templated Grain Growth, Journal of the American Ceramic Society 83 (2000) 3109–3116. https://doi.org/10.1111/j.1151-2916.2000.tb01690.x.

[35] M.N. Rahaman, Sintering of Ceramics, Taylor and Francis, Hoboken, 2007.

[36] R.M. German, P. Suri, S.J. Park, Review: liquid phase sintering, J Mater Sci 44 (2009) 1–39. https://doi.org/10.1007/s10853-008-3008-0.

[37] J. Wang and R. Stevens, Zirconia-toughened alumina (ZTA) ceramics, J Mater Sci 24 (1989) 3421–3440.

[38] Ronald G. Munro, Evaluated Material Properties for a Sintered alpha-Alumina, J. Am. Ceram. Soc. 80 (1997) 1919–1928.

[39] W. E. Lee and W. M. Rainforth, Ceramic Microstructures, Chapman & Hall, London, 1994.

[40] P. Auerkari, Mechanical and physical properties of engineering alumina ceramics, Technical Research Centre of Finland (1996).

[41] J. Eichler, U. Eisele, J. Rödel, Mechanical Properties of Monoclinic Zirconia, Journal of the American Ceramic Society 87 (2004) 1401–1403. https://doi.org/10.1111/j.1151-2916.2004.tb07748.x.

[42] ÖNORM, Hochleistungskeramik - Prüfverfahren zur Bestimmung der Bruchzähigkeit monolothischer Keramik: Verfahren für Biegeproben mit V-Kerbe (SEVNB-Verfahren), 2016.

[43] T. Nishida, Y. Hanaki, G. Pezzotti, Effect of Notch-Root Radius on the Fracture Toughness of a Fine-Grained Alumina, J American Ceramic Society 77 (1994) 606–608. https://doi.org/10.1111/j.1151-2916.1994.tb07038.x.

[44] ÖNORM, Hochleistungskeramik - Mechanische Eigenschaften monolithische Keramik bei Raumtemperatur: Teil 1: Bestimmung der Biegefestigkeit, 2008.

[45] F.K. Lotgering, Topotactical reactions with ferrimagnetic oxides having hexagonal crystal structures—I, J. Inorg. Nucl. Chem 9 (1959) 113–123.

[46] M.D. Vaudin, M.W. Rupich, M. Jowett, G.N. Riley, J.F. Bingert, A method for crystallographic texture investigations using standard x-ray equipment, J. Mater. Res. 13 (1998) 2910–2919. https://doi.org/10.1557/JMR.1998.0398.

[47] ÖNORM, Hochleistungskeramik - Monolithische Keramik-Allgemeine und strukturelle Eigenschaften: Teil 2: Bestimmung von Dichte und Porosität, 1994.

[48] ÖNORM, Hochleistungskeramik - Mechanische Eigenschaften monolithische Keramik bei Raumtemperatur: Teil 2: Bestimmung des Elastizitätsmoduls, Schubmuduls und der Poissonzahl.

[49] ÖNORM, Hochleistungskeramik -Mechanische Eigenschaften monolithische Keramik bei Raumtemperatur: Teil 4: Härteprüfung nach Vickers,Knoop und Rockwell, 2005.

[50] DIN, Hochleistungskeramik - Prüfverfahren zur Bestimmung der Bruchzähigkeit monolithischer Keramik bei Raumtemperatur an einseitig gekerbten Biegeproben (SEPB-Verfahren), 2005.

[51] M. Zhang, Y. Chang, R. Bermejo, G. Jiang, Y. Sun, J. Wu, B. Yang, W. Cao, Improved fracture behavior and mechanical properties of alumina textured ceramics, Mater. Lett. 221 (2018) 252–255.

[52] J.A. Choren, S.M. Heinrich, M.B. Silver-Thorn, Young's modulus and volume porosity relationships for additive manufacturing applications, J Mater Sci 48 (2013) 5103–5112. https://doi.org/10.1007/s10853-013-7237-5.

[53] Mc Colm, Ceramic Hardness, Plenum Press, New York (1990).

[54] T. Carisey, I. Levin, and D.G. Brandon, Microstructure and mechanical properties of textured Al2O3, J. Eur. Ceram. Soc. 283 (1995).

[55] M. Iwasa, R. C. Brandt, Fracture Toughness of Single-Crystal Alumina, Advances in ceramics 1984 767–774.

[56] W. Weibull (Ed.), A Statistical Theory of the Strength of Materials, Generalstabens litografiska anstalts forlag, Stockholm, 1939.

[57] W. Weibull, A statistical distribution function of wide applicability, J. Appl. Mech. (1951) 293–297.

[58] Munz, D. and Fett, T., Ceramics. Mechanical Properties, Failure Behaviour, Materials Selection, Materials science 36 (2001).

[59] Yu.V. Milman a, S.I. Chugunova, I.V. Goncharova, W. Gooch, Temperature dependence of hardness in silicon±carbide ceramics with dierent porosity, International Journal of refractory metals and hard materials 17 (1999) 361–368.